PHYSICS OF FLUIDS **30**, 013602 (2018)

Central recirculation zones and instability waves in internal swirling flows with an annular entry

Yanxing Wang and Vigor Yang[a)]
School of Aerospace Engineering, Georgia Institute of Technology, Atlanta, Georgia 30332, USA

(Received 20 August 2017; accepted 15 December 2017; published online 18 January 2018)

The characteristics of the central recirculation zone and the induced instability waves of a swirling flow in a cylindrical chamber with a slip head end have been numerically investigated using the Galerkin finite element method. The effects of Reynolds number as well as swirl level adjusted by the injection angle were examined systematically. The results indicate that at a high swirl level the flow is characterized by an axisymmetric central recirculation zone (CRZ). The fluid in the CRZ takes on a solid-body rotation driven by the outer main flow through a free shear layer. Both the solid-body rotating central flow and the free shear layer provide the potential for the development of instability waves. When the injection angle increases beyond a critical value, the basic axisymmetric flow loses stability, and instability waves develop. In the range of Reynolds numbers considered in this study, three kinds of instability were identified: inertial waves in the central flow, and azimuthal and longitudinal Kelvin-Helmholtz waves in the free shear layer. These three types of waves interact with each other and mix together. The mode selection of the azimuthal waves depends strongly on the injection angle, through the perimeter of the free shear layer. Compared with the injection angle, the Reynolds number plays a minor role in mode selection. The flow topologies and characteristics of different flow states are analyzed in detail, and the dependence of flow states on the injection angle and Reynolds number is summarized. Finally, a linear analysis of azimuthal instabilities is carried out; it confirms the mode selection mechanisms demonstrated by the numerical simulation. *Published by AIP Publishing.* https://doi.org/10.1063/1.5000967

I. INTRODUCTION

One characteristic of the swirling flow is the formation of a central recirculation zone (referred to here as CRZ) downstream of the swirling vanes, which plays an important role in combustion devices to improve flame stabilization and enhance mixing of fuels and oxidizers.[1–3] The CRZ can be created by several methods in swirling systems, including strengthening swirl at the flow entrance, applying sudden expansion on the sidewalls, and placing a central bluff body on the axis. In most devices, one or more of these methods is used jointly for optimal control of flow and flame behaviors. Although considerable efforts have been made in this area in past decades, the mechanisms and flow characteristics of the CRZ are still poorly understood, even for a simple flow in a cylindrical chamber. The difficulties generally lie in the complexity of the coupling of various mechanisms, subject to a broad range of flow parameters.

When fluid is injected into a cylindrical chamber with such a high swirl level that the centrifugal effect dominates over other effects, the centrifugal force drives the fluid outward to the sidewalls and creates an axisymmetric bubble-like or column-like "cavity" on the axis. This "cavity" is the simplest CRZ and is commonly observed in many swirling devices.[4–7] Previous studies have found that this kind of CRZ only occurs when the swirl number [refer to Eq. (7)] exceeds a critical value S_{crit}.[1,2] Gupta *et al.*[2] showed that S_{crit} is about 0.6 for the flow in a cylindrical chamber. This conclusion provides an important criterion for the occurrence of the CRZ.

Experimental measurements[1–3,8] have shown that the axisymmetric CRZ driven by the centrifugal force at a high swirl level is enveloped by a free shear layer, across which the tangential and axial velocities change significantly. This layer, with its sharp velocity gradient, provides the potential for shear instability to develop. As the basic state loses stability, the axisymmetric flow structure breaks up into a periodic wave-like pattern aligned in the azimuthal and axial directions. This inspires us to ask whether the instability waves and the mechanisms of mode selection provide the links connecting different flow states.

The earliest study of the instability of the free shear layer in the swirling flow is by Hide and Titman.[9] They dealt with the free shear layer (called the "detached shear layer" in their paper) created by a rotating disk placed in a cylindrical container with different rotation speed. In their experiments, the flow consists of a free shear layer, which is fundamentally a Stewartson layer together with an Ekman boundary layer on the rotating disk.[10,11] Their results show that the flow pattern is determined by both Rossby number

$$Ro \equiv \frac{(\Omega_1 - \Omega_0)}{(\Omega_1 + \Omega_0)/2} \tag{1}$$

and Ekman number

$$E \equiv \frac{2\nu}{R^2\,(\Omega_1 + \Omega_0)}, \tag{2}$$

[a)]Author to whom correspondence should be addressed: vigor.yang@aerospace.gatech.edu

where Ω_0 and Ω_1 are the angular velocities of the cylindrical container and the rotating disk, R is the radius of the disk, and ν is the kinematic viscosity of fluid. When the Rossby number is below a critical value, the flow exhibits axisymmetric characteristics. Otherwise, when the Rossby number exceeds the critical value, a wave-like non-axisymmetric pattern appears and the wave number decreases with the amplitude of the difference in rotation speed. Rabaud and Couder[12] pointed out that the wave phenomena observed in the experiments of Hide and Titman[9] are not a simple Kelvin-Helmholtz instability; the centrifugal force and the Coriolis force also play non-negligible roles. According to the theory of Niino and Misawa,[13] the stability of the Stewartson layer is determined by the Reynolds number, defined based on the velocity difference across the free shear layer and the thickness of the Stewartson $E^{1/4}$-layer. They find that the wave number decreases with increasing Reynolds number, which is opposite to the common analysis that the most unstable wave number increases with the Reynolds number. This conclusion was confirmed by Konijnenberg *et al.*,[14] who performed experiments on the free shear layer created in a parabolic vessel with a differentially rotating central section. Their observation is in agreement with the relationship between the wave number and Reynolds number obtained by many other researchers for different flow conditions.[15,16]

The free shear layers in the previously mentioned studies were created by the rotation of one or two solid disks and were connected with the Ekman layer on the rotating disks. In contrast to these studies, the free shear layer in a cylindrical chamber is created by tangentially injected fluid, and the flow parameters related to the free shear layer, such as the layer thickness and the angular velocities inside and outside the layer, are not well defined.

In most swirling devices with injection ports on the sides, a stationary solid plate is placed at the head end of the chamber. In the boundary layer formed on the end surface, the azimuthal velocity of the flow is reduced due to viscous dissipation, and the equilibrium between the radial pressure gradient and the centrifugal force is broken. The excessive pressure gradient drives the fluid in the boundary layer to the axis and gives rise to a jet-like flow on the axis. The interaction with this jet flow causes the CRZ and instability waves to behave distinctively and develop some complicated nonlinear phenomena.

As the first step in a series of studies to fully understand the physics of CRZs and the instability waves developed in the swirling flow, and to understand the connections between the different flow states over a variety of swirl levels and Reynolds numbers, we initiate this exploration into the behaviors of CRZ and the instability waves in a cylindrical vortex chamber with a *slip* head end. The purpose of eliminating the friction on the end surface is to identify the centrifugal effect and examine the flow and instability characteristics in the absence of the boundary flow due to friction on the head end. When the slip head end is considered as the symmetry plane, the flow is identical to that injected into a cylindrical chamber through an annular entrance located halfway along the cylinder.

In this paper, we present a numerical model to simulate the swirling flow in a cylindrical chamber with a slip head end. A flow is injected into the cylinder through an annular entrance on the sidewall near the head end. A flow swirl is introduced aerodynamically by controlling the injection flow angle. The overall objectives of the present study are multiple. The first is to systematically investigate the flow features of the CRZ driven by the centrifugal force and the characteristics of the instability waves developing in the free shear layer enveloping the CRZ, and to offer insight into the mechanisms governing the flow evolution. The second is to establish the connections between different states in a broad range of swirl numbers and Reynolds numbers. This paper is organized as follows. In Sec. II, detailed descriptions of the physical models are presented. In Sec. III, the numerical model and approaches are described. The results are discussed in Sec. IV. Section V offers conclusions.

II. PHYSICAL MODEL

In order to avoid the complexity caused by device configuration, we adopt a highly simplified swirl geometry, with dynamics similar to those of the above-mentioned studies. As shown in Fig. 1, the present geometry includes a long cylindrical chamber of diameter D with an annular entrance on the side at the head end. The width of the entrance is denoted by d. Fluid is injected into the chamber through the entrance with uniform radial velocity $U_{r,in}$ and tangential velocity $U_{\theta,in}$. The injection angle is defined as the angle between the injection velocity vector and the tangent of the cylindrical chamber, $\theta_{in} = \tan^{-1}(U_{r,in}/U_{\theta,in})$. The radial velocity component can be acquired from $U_{\theta,in}$ and θ_{in}. Thus, a complete description of the swirling flow in the cylinder includes D, d, θ_{in}, $U_{\theta,in}$, and ν, where ν is the kinematic viscosity of the fluid in the chamber.

In most studies, the Reynolds number is defined based on the mean axial velocity in the cylinder as $\mathrm{Re}_x = \bar{u}_x D/\nu$, where $\bar{u}_x$ is the mean axial velocity and D is the chamber diameter. In the present study, however, the swirl effects are closely related to the tangential velocity at the entrance, so we choose the injection tangential velocity $U_{\theta,in}$ and the cylinder diameter D as the characteristic variables and define the Reynolds number as

$$\mathrm{Re}_\theta = \frac{U_{\theta,in} D}{\nu}. \tag{3}$$

The relationship between this tangential Reynolds number and the conventional Reynolds number based on the mean axial velocity is

$$\mathrm{Re}_x = \frac{4d}{D} \tan\theta_{in} \cdot \mathrm{Re}_\theta. \tag{4}$$

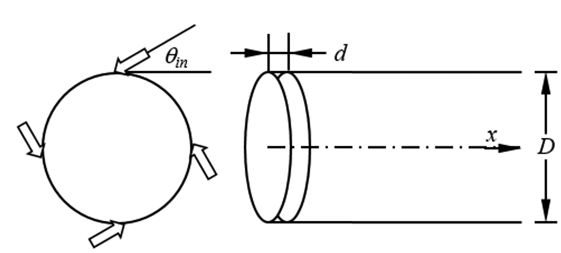

FIG. 1. Configuration: cylindrical container with an annular entry.

Here, we consider only the laminar flow with Re_θ ranging from 100 to 3000. In the simulation, the velocity and length scales are normalized with the tangential velocity of the injection flow $U_{\theta,in}$ and the radius of the cylindrical chamber R. In the nondimensional form, $U_{\theta,in} = 1$ and $D = 2$. The controlling parameters for the present configuration reduce to d, θ_{in}, and Re_θ. The angular momentum carried by a unit volume of fluid at the entrance is

$$M = U_{\theta,in} D/2 = 1. \tag{5}$$

The volumetric flow rate injected into the chamber is

$$\dot{V} = U_{\theta,in} \tan\theta_{in} \cdot \pi D d = 2\pi d \tan\theta_{in}. \tag{6}$$

The immediate consequence of increasing the injection angle θ_{in} is an increase in the volume flow rate and the angular momentum flux into the chamber. The swirl level, characterized by the swirl number, is defined as

$$S = \frac{\int_A \rho u_\theta r \cdot u_x dA}{D/2 \cdot \int_A \rho u_x \cdot u_x dA}, \tag{7}$$

where ρ is the fluid density, u_θ is the azimuthal velocity, u_x is the axial velocity, and A is the cross-sectional area at any axial location of the cylinder. The swirl number S is a nondimensional number representing the ratio of the axial flux of angular momentum to the axial flux of axial momentum. For the present configuration, fluid is injected into the chamber with zero axial velocity, so we need to define an equivalent swirl number to avoid dividing by the zero axial velocity in estimating the swirl number of the injected flow. An approximate method is to employ the averaged axial velocity $\bar{u}_x$ obtained from the volume flow rate injected into the chamber and assume that the angular momentum is perfectly conserved. The swirl number of the injected flow is then

$$S_{in} = \frac{R}{2d}\frac{1}{\tan\theta_{in}}, \tag{8}$$

where $R = 1$ in the nondimensional form. This expression implies that for a given geometry the injection swirl number S_{in} is inversely proportional to the tangent of injection angle θ_{in}. The increasing injection angle θ_{in} will lead to the decrease in swirl level of the injection flow. This is because, although the increase in θ_{in} increases the axial fluxes of both angular momentum and axial momentum, the ratio of these two fluxes decreases. This conclusion is only valid for the injected flow in a limited upstream regime because viscous dissipation tends to decrease the flow swirl, and the variation of swirl number also depends on the specific flow characteristics. In this study, the nondimensional entrance width d is fixed at 0.2. The swirl numbers of the injected flow at various angles considered in this study are listed in Table I.

TABLE I. Swirl number of the injected flow with various vane angles.

θ_{in} (deg)	10	20	30	45	55	60	75
S_{in}	14.18	6.87	4.33	2.50	1.75	1.44	0.67

III. GOVERNING EQUATIONS AND NUMERICAL METHODS

Under the assumption that the flow is laminar, three-dimensional, and incompressible, the non-dimensional conversation equations based on the tangential velocity of injection flow $U_{\theta,in}$ and chamber radius R can be written as

$$\nabla \cdot \mathbf{u} = 0, \tag{9}$$

$$\frac{\partial \mathbf{u}}{\partial t} + \mathbf{u} \cdot \nabla \mathbf{u} = -\nabla p + \frac{2}{\mathrm{Re}_\theta}\nabla^2 \mathbf{u}, \tag{10}$$

where Re_θ is the Reynolds number defined by Eq. (3), $\mathbf{u}$ is the velocity vector, and p is the nondimensional pressure ($p \equiv \tilde{p}/\rho U_{\theta,in}^2$, $\tilde{p}$ is the pressure with units). A slip condition is used on the head end, a non-slip condition is used on the sidewall, and an out-flow condition is used at the downstream end of the chamber. At the annular entrance, the inlet condition is specified as

$$u_\theta = U_{\theta,in} = 1, \tag{11}$$

$$u_r = U_{r,in} = U_{\theta,in} \tan\theta_{in}. \tag{12}$$

In this paper, a finite element solution for a three-dimensional incompressible viscous flow is considered. Discretization in space is carried out by the Galerkin weighted residual method.[17] For time advancement, the velocity correction method (explicit forward Euler), given in detail by Kovacs and Kawahara,[18] is employed. The method gives results of the second order of accuracy in both time and space.

In the simulations, the axial length of the computational domain is 30 times as long as the cylinder radius. For a laminar flow, this length is long enough to make the influence on the interior flow from the downstream boundary negligible.

In order to check the grid sensitivity of the numerical results, two flows with injection angle $\theta_{in} = 10°$ and $45°$ at $\mathrm{Re}_\theta = 1000$ were simulated with three grid systems: fine grid 4205×150 (cross section $\times$ axis), medium grid 1125×75, and coarse grid 245×75. The profiles of azimuthal and radial velocities on the slip head end with different grid resolutions are shown in Fig. 2. At $\theta_{in} = 45°$, flow instability appears, and the azimuthally averaged velocity components are shown in the figure. A comparison of the curves shows that for azimuthal velocity u_θ, the largest deviation occurs at the outer and inner boundaries of the free shear layer, where u_θ changes abruptly. For radial velocity u_r, the deviation primarily appears in the central region. Please refer to Sec. IV for a detailed discussion of the flow patterns. These curves demonstrate excellent convergence as the grid resolution improves from the medium grid to fine grid. In our simulation, the fine grid is used for all cases with $\mathrm{Re}_\theta \le 1000$, to support the accuracy of the numerical results. For $\mathrm{Re}_\theta > 1000$, an extra fine grid 6125×150 is adopted. Under different conditions, the distribution of grid nodes is adjusted according to the gradients of flow quantities.

The velocities of a flow with uniform axial velocity and zero azimuthal velocity are used as the initial conditions. Over time, the flow gradually enters a quasi-steady state in which all variables change periodically with time. Our analysis is conducted in the quasi-steady state.

The details of the numerical method with validation tests can be found in the studies of Wang *et al.*[19,20]

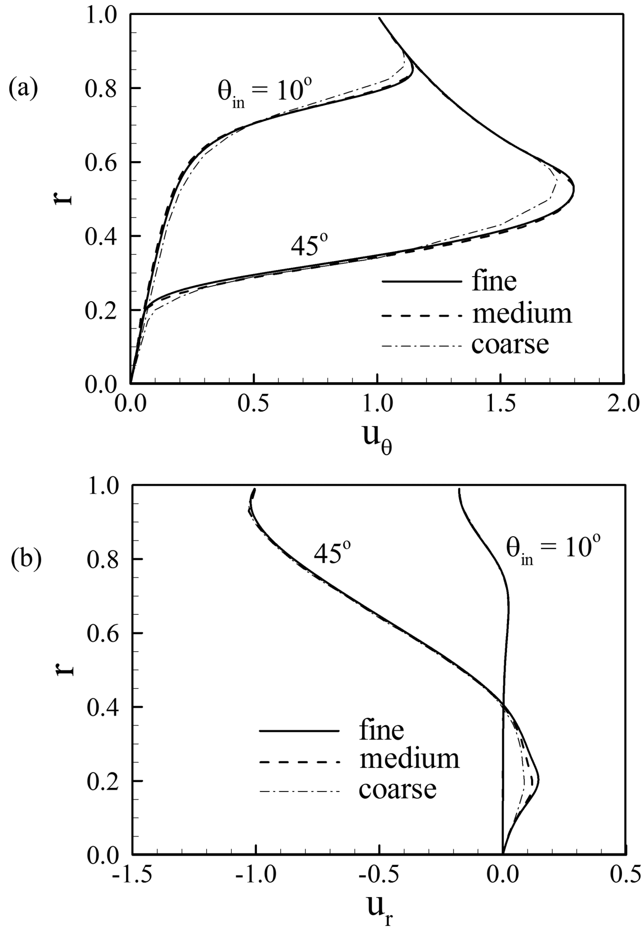

FIG. 2. Effect of grid resolution on azimuthal and radial velocity on the slip head end at $Re_\theta = 1000$. The azimuthally averaged u_θ is shown. (a) Azimuthal velocity and (b) radial velocity.

IV. RESULTS AND DISCUSSION

For a given configuration, the flow evolution in the chamber is determined by the injection swirl number S_{in} and tangential Reynolds number Re_θ. In the following analysis, the axisymmetric basic flow without instability wave will be discussed first. This kind of flow typically occurs at high swirl levels and low Reynolds numbers. After that, the instability waves in the free shear layer at low swirl levels will be discussed. Overall, the injection angle θ_{in} increases from 10° to 75°. Correspondingly, the injection swirl number S_{in} decreases from 14.18 down to 0.67 (Table I). The azimuthal Reynolds number Re_θ ranges from 100 to 3000, and the analysis is limited to the laminar flow range.

A. Axisymmetric columnar central recirculation zone at high swirl level and low Reynolds number

At a high swirl level, the centrifugal effect is dominant over the other effects, and the flow is characterized by an axisymmetric column-like or bubble-like recirculation zone on the axis. When fluid is injected into the chamber, the strong centrifugal force drives the fluid outward and forces it to travel along the sidewall in a spiral path downstream. This flow motion creates an axisymmetric cylindrical recirculation zone on the axis when the Reynolds number is not too small. Such recirculation zone is referred to as the "central recirculation zone" (CRZ). It can be easily seen that the motion of fluid in the CRZ is driven by the outer downstream traveling flow newly injected into the chamber. We use a flow at $\theta_{in} = 20°$ and $Re_\theta = 300$ as an example to demonstrate the basic flow patterns in Fig. 3.

Figures 3(a) and 3(b) show the typical three-dimensional streamlines of the central recirculating flow and the outer main flow, respectively. In the quasi-steady state, the streamlines coincide with the trajectories of fluid particles. As shown in these two figures, both the outer and central flows travel in a spiral manner, as is commonly observed in swirl devices. The CRZ can be clearly identified in Fig. 3(c), which shows the projected streamlines on the central plane along the axis. When the Reynolds number is not too high, the flow stays stable to azimuthal disturbances and the flow patterns remain axisymmetric. The streamlines in the CRZ are closed and only recirculate within the central region.

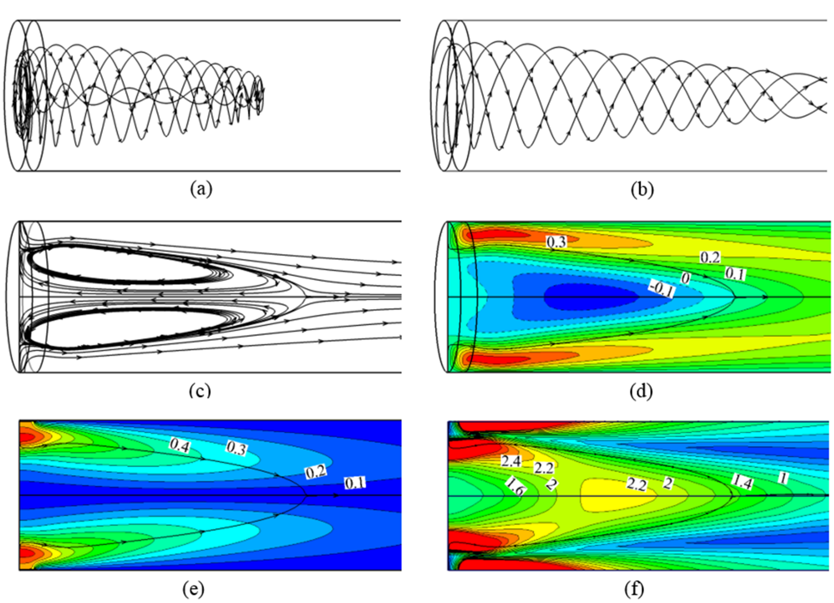

FIG. 3. Overview of swirling flow with columnar CRZ in a cylindrical chamber with the slip head end at $\theta_{in} = 20°$ and $Re_\theta = 300$. (a) Typical streamlines in the CRZ; (b) typical streamlines outside the CRZ; (c) projected streamlines on the x-y plane; (d) contours of axial velocity u_x on the x-y plane; (e) contours of azimuthal velocity u_θ on the x-y plane; (f) contours of vorticity magnitude $|\omega|$ on the x-y plane.

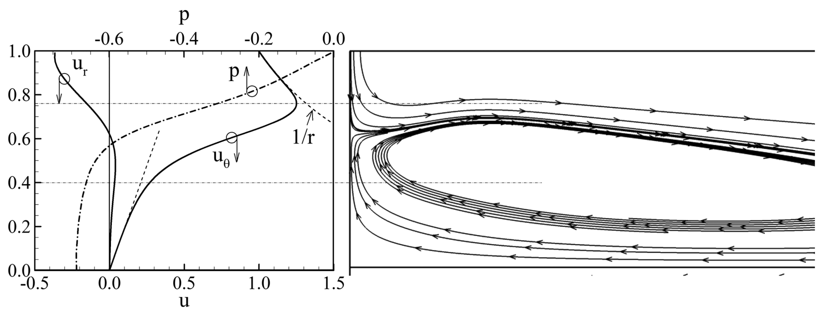

FIG. 4. Profiles of azimuthal and radial velocity components and pressure on the slip head end at $\theta_{in} = 20°$ and $Re_\theta = 300$.

The contours of axial and azimuthal velocities on the central plane are shown in Figs. 3(d) and 3(e). Both velocity components reach their maxima in the outer downstream-traveling flow. In the contours of vorticity magnitude shown in Fig. 3(f), a free shear layer with a concentrated vorticity magnitude can be observed at the interface of the outer and central flows. In the three-dimensional pattern, this layer shows up as a cylindrical structure. The presence of this free shear layer, as well as the distributions of axial and azimuthal velocities, suggests that the motion of the central recirculating flow is driven by the outer downstream traveling flow by means of shear stress.

The interactions between the outer and central flows are examined through the profiles of velocity components and pressure on the slip head end shown in Fig. 4. The distribution of the azimuthal velocity u_θ implies that the flow near the head end can be decomposed into three consecutive regimes along the radius. The outer regime is occupied by the flow that has just entered the chamber, and the angular momentum is well conserved, and the change of azimuthal velocity satisfies $u_\theta r = U_{\theta,in} R = 1$. Therefore, the outer layer can be considered as a potential flow regime before the friction on the sidewalls takes effect downstream. In the central regime occupied by the central recirculating flow, the azimuthal velocity exhibits linear dependence on the radial coordinate, which means that the flow in the central regime takes on a solid-body rotation.

The azimuthal velocity decreases sharply between the outer and central regimes, from the outer potential flow to the central solid-body rotating flow. A free shear layer exists between the outer and central flows, indicating that the motion of the CRZ is driven by the outer main flow by means of shear stress. The radial velocity u_r shows a monotonic decrease in magnitude from the entrance to the separation point where $u_r = 0$. The separation point is located in the free shear layer. It should be noted that the magnitude of radial velocity of the CRZ is much smaller than that of the outer flow. This implies that the passive motion of the central recirculating flow is not as strong as the outer flow. In the swirling flow, the centrifugal force is roughly balanced by the radial pressure gradient. In this figure, the sharp decrease in pressure outside the CRZ confirms that the swirl motion of the outer flow is much stronger than the central solid-body rotation.

The profiles of azimuthal and axial velocities at different axial locations are given in Figs. 5(a) and 5(b). A sharp decrease in the azimuthal velocity takes place between the outer potential flow and the central solid-body rotating flow at $x = 0$, which indicates the presence of the free shear layer. However, at $x = L_{CRZ}/2$, where L_{CRZ} is the length of the CRZ, this sharp decrease in u_θ can no longer be seen on the curve. This is because the free shear layer is created in the upstream region and only extends a limited distance downstream because of viscous dissipation. The free shear layer provides the environment for the development of Kelvin-Helmholtz instability waves in the azimuthal and longitudinal directions in the upstream region. Comparing the u_θ profiles at $x = 0$ and $x = L_{CRZ}/2$, the slope of the curve in the central regime at $x = L_{CRZ}/2$ is bigger than that at $x = 0$, which means that the CRZ swirls faster in the downstream section. This is consistent with the contours of u_θ shown in Fig. 3(e); in the process of traveling downstream, the outer main flow continuously transfers angular momentum to the CRZ until a balance point is reached. As a result, the CRZ rotates faster in the downstream region. According to the criterion for inertial waves,[21] the solid-body rotation of the CRZ provides the potential for the development of inertial waves in the central region. We will discuss this issue in Sec. IV B of this paper. Due to viscous dissipation, the swirl strength decreases as the flow moves downstream. At $x = 2L_{CRZ}$, the swirl is almost fully dissipated.

The axial velocity vanishes on the axis at the downstream end of the CRZ. Inside the CRZ, $u_x < 0$ along the axis. At each axial location, the axial velocity reaches a peak in the outer main flow. As the outer flow travels downstream, the peak eventually shifts toward the axis. At about $x = 2L_{CRZ}$, the

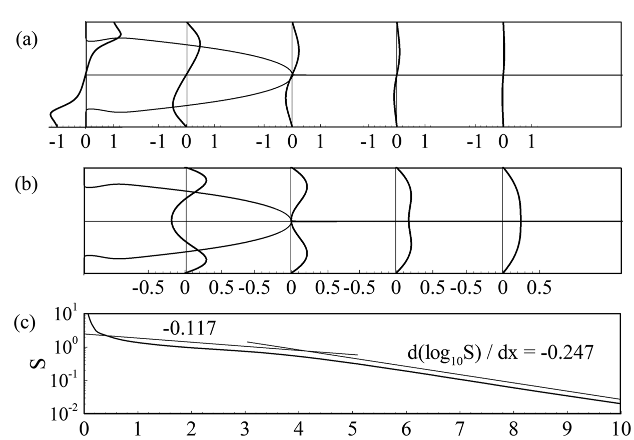

FIG. 5. Profiles of (a) azimuthal and (b) axial velocity components at x/L_{CRZ} = 0, 0.5, 1, 1.5, and 2 and (c) axial variation of swirl number at $\theta_{in} = 20°$ and $Re_\theta = 300$.

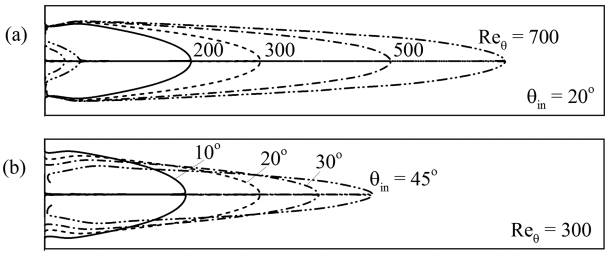

FIG. 6. Profiles of CRZ on the x-y plane at different injection angles and Reynolds numbers: (a) θ_{in} = 20° and (b) Re_θ = 300.

axial velocity peak arrives at the axis. The axial variation of swirl number in logarithm scale is given in Fig. 5(c). The curve can apparently be split into two straight lines connecting at the end point of the CRZ. The slopes of the curves are $d(\log_{10} S)/dx = -0.117$ and -0.247 in the upstream region occupied by the CRZ and in the downstream region, respectively. This curve clearly shows that the variation of flow swirl is subject to a linear relationship with the axial coordinate and demonstrates that the behaviors of the CRZ are governed by linear mechanisms.

It is known that the evolution of the CRZ driven by the centrifugal force is directly related to the axial variation of flow swirl.[2] Such evolution only appears, however, when the swirl number exceeds a critical value. In the present configuration, the variation of flow swirl depends on the swirl number at the entrance S_{in} and the swirl Reynolds number Re_θ. S_{in} is determined by injection angle θ_{in} through Eq. (6). Figure 6 shows the influence of Reynolds number Re_θ and injection angle θ_{in} on the profile of the CRZ. At higher Reynolds numbers, the flow swirl is dissipated more slowly than at lower Reynolds numbers. Consequently, the CRZ extends farther downstream. This phenomenon is confirmed by Fig. 6(a), which shows the profiles of the CRZ at Re_θ from 200 to 700 and θ_{in} = 20°. On the other hand, a larger injection angle has a higher volume flow rate through the entrance, in the nondimensional form. We have shown in Eq. (5) that angular momentum carried by a unit volume of fluid is constant. Therefore, the increased flow rate of angular momentum due to the increase in injection angle will result in an axial elongation of the CRZ. This is consistent with the profiles of CRZ at different θ_{in}, shown in Fig. 6(b). These two figures also show that the position of the separation point on the head end is not sensitive to the Reynolds number, and it appears to shift to the axis as the injection angle increases. In fact, the position of the separation point and the radial location of the free shear layer are primarily determined by the radial momentum of the injection flow. Higher radial momentum at a larger injection angle pushes the separation point closer to the axis.

Figure 7 shows comparisons of azimuthal and radial velocity components and pressure on the slip head end at various Reynolds numbers and injection angles before the flow loses stability. In Fig. 7(a), as we observed in Fig. 4, the azimuthal velocity obeys the conservation of angular momentum in the outer main flow for all cases, $u_\theta r = U_{\theta,in} R = 1$. In the central regime, the CRZ takes on a solid-body rotation, for which the azimuthal velocity changes linearly with the radial coordinate. The outer main flow and the central recirculating flow are connected by a free shear layer, in which the azimuthal velocity undergoes a sharp change. With the increase in injection angle, the free shear layer shifts toward the axis and the rotation speed of the CRZ increases. At any given injection angle, the higher Reynolds number has a thinner free shear layer and a smaller angular velocity of the solid-body rotation of the CRZ.

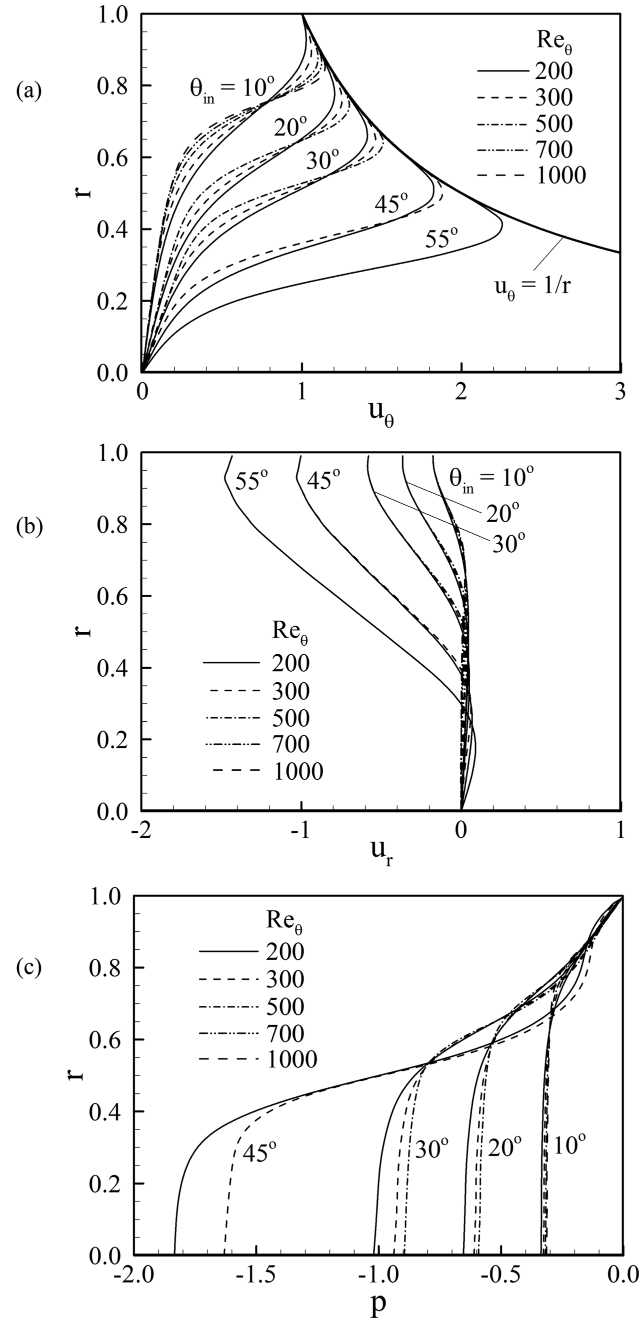

FIG. 7. Profiles of (a) azimuthal and (b) radial velocity components and (c) pressure on the slip head end at different θ_{in} and Re_θ, in the axisymmetric flow regime.

The radial velocity shown in Fig. 7(b) is not as sensitive to the Reynolds number in the outer regime. The magnitude $|u_r|$ in the outer main flow is always larger than that in the CRZ. With the increase in injection angle, $|u_r|$ increases in both the outer main flow and the central recirculating flow. This is natural since the velocity is normalized with the tangential velocity at the entrance.

As shown in Fig. 7(c), the pressure decreases significantly over the outer flow and the free shear layer from the entrance and remains largely constant in the central regime. As the free shear layer shifts to the axis with increasing injection angle, the pressure in the central regime decreases correspondingly. For a given injection angle, the higher Reynolds number has a thinner free shear layer. As a result, the central pressure is relatively higher.

The column-like or bubble-like CRZ only occurs when the swirl number S exceeds a critical value S_c and ends at the position where S becomes smaller than S_c.[2] Therefore, the longitudinal length of the recirculation zone L_{CRZ} largely reflects the resistance of the flow to swirl dissipation. It is apparent that the higher Reynolds number allows a lower dissipation rate, and the larger injection angle produces a higher flow rate of angular momentum, both of which lead to a longer CRZ.

Figure 8 shows the dependence of the length of CRZ on the Reynolds number Re_θ and the injection angle θ_{in}. The horizontal and vertical axes are both in logarithmic scale. Figure 8(a) illustrates a linear relationship between L_{CRZ} and Re_θ in logarithm scale, regardless of the injection angle. Figure 8(b) exhibits another linear relationship between L_{CRZ} and θ_{in}, with roughly the same slope for different Re_θ when θ_{in} is not high. At higher injection angles ($\theta_{in} \geq 45°$), the flow injected with higher radial momentum is pushed to the outer region before it reaches the axis. Such motion of the injected flow forms a wavy pattern and tends to terminate the CRZ before the swirl number is decreased to the critical value. As a result, L_{CRZ} is smaller than that predicted by the linear relationship at a higher injection angle. The linear relationships in this figure suggest a general expression of L_{CRZ} in terms of Re_θ and θ_{in},

$$L_{CRZ} = c\,\mathrm{Re}_\theta^a\,\theta_{in}^b, \tag{13}$$

where a, b, and c are constants and depend only on the geometry of the chamber.

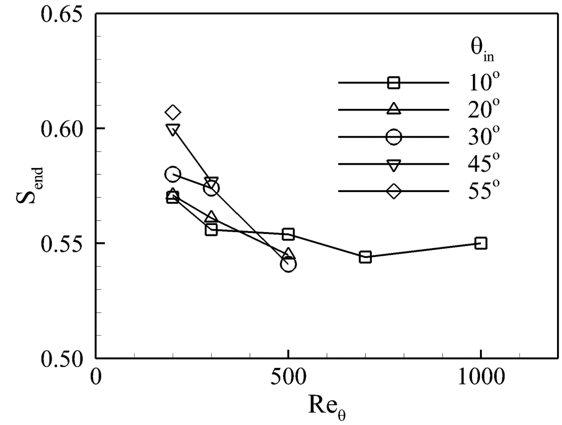

FIG. 9. Swirl numbers at the end of the CRZ.

Figure 9 gives the swirl number at the end point of the CRZ at different injection angles and Reynolds numbers, equivalent to the critical swirl number S_c in the literature. In this figure, S_{end} does not remain constant for our cases and shifts in the range from 0.54 to 0.61, which is close to the experimental measurement $S_{end} = 0.6$ of Gupta *et al.*[2] By and large, the plot displays a decreasing trend of S_{end} with Re_θ for all the injection angles under consideration. At a given Re_θ, S_{end} is slightly larger for higher θ_{in}. This phenomenon is caused by the bouncing effect at higher θ_{in} introduced in the discussion of Fig. 8, which tends to terminate the CRZ before the swirl number decreases to the value of those at lower θ_{in}.

At the downstream end of the CRZ, the swirl number falls into a narrow range for all injection angles and Reynolds

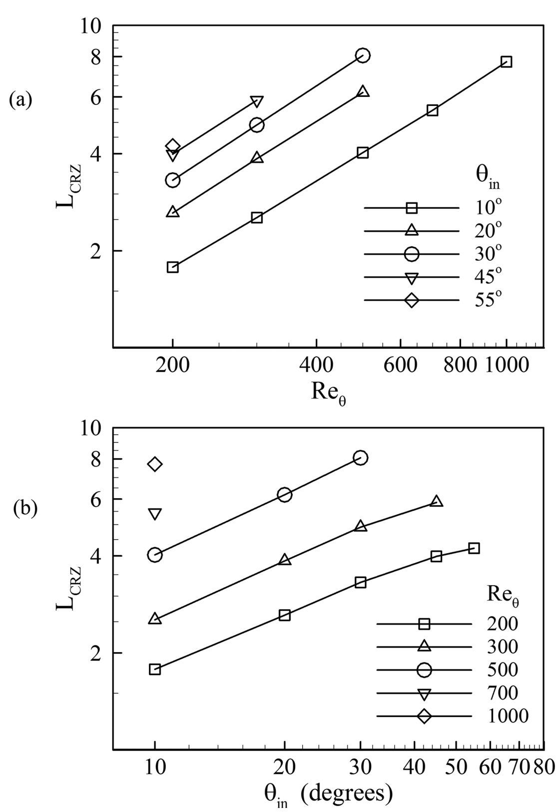

FIG. 8. Dependence of the length of the CRZ on (a) Reynolds number Re_θ and (b) injection angle θ_{in}.

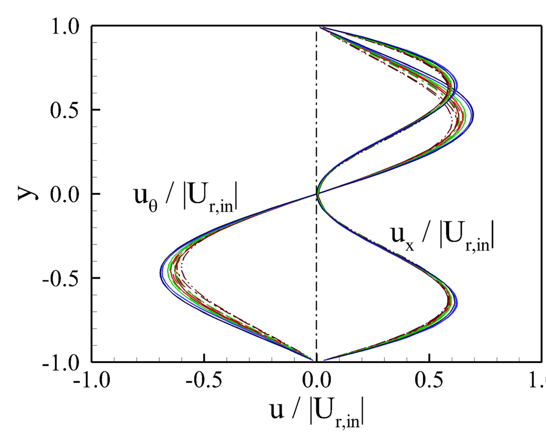

FIG. 10. Distribution of axial and azimuthal velocities at the end of the CRZ (normalized by injection radial velocity at entrance). Brown, $\theta_{in} = 10°$; red, 20°; green, 30°; blue, 45°; dark blue, 55°. Solid, $\mathrm{Re}_\theta = 200$; dash, 300; dashdot, 500; dashdotdot, 700.

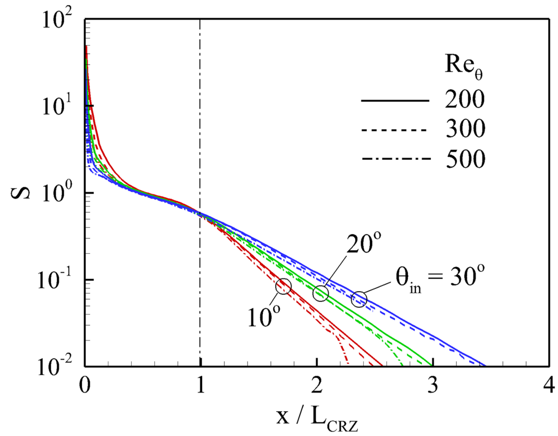

FIG. 11. Variation of swirl number along the axis. The axial coordinate normalized by the length of central recirculation zone L_{CRZ}.

numbers, which inspires us to ask whether the distributions of axial and azimuthal velocity components might have similar features for different flow conditions. Figure 10 shows the profiles of axial and azimuthal velocities at the end of the CRZ at different θ_{in} and Re_θ. To accommodate the discrepancies of the volume flow rate caused by the injection angle, the velocities in this plot are normalized by the radial component of injection velocity, which is expressed as $U_{r,in} = U_{\theta,in} \tan\theta_{in}$. For both axial and azimuthal velocities, the curves are close to each other and collapse in places onto a single curve. This implies that in the basic swirling flow the velocity distributions might be described by a self-similar expression in terms of injection swirl number.

The axial variation of swirl number at different injection angles and Reynolds numbers is shown in Fig. 11. The axial coordinate is normalized with the length of the CRZ for each case. It is not surprising that the curves are collapsed onto a single straight line in the region of the CRZ, except at the beginning section near the head end. In the downstream region, these curves remain straight, but the slopes become different. This deviation is mainly related to the injection angle. As the injection angle increases from 10° to 30°, the slope of the curve decreases in the downstream region. This plot confirms the conclusion that the occurrence of the CRZ is governed by log-linear mechanisms. Using Figs. 8–11, a series of linear and log-linear correlations can be developed to fully describe the characteristics of the swirling flow with a CRZ. In other words, the behaviors of this kind of flow are predictable.

B. Columnar central recirculation zone with instability waves at medium swirl level

At a low injection angle, an axisymmetric CRZ develops on the axis as a result of high swirl. The free shear layer between the outer main flow and the central recirculating flow provides the potential for instabilities to grow. At a low injection angle ($\theta_{in} < 30°$), the free shear layer is close to the side-wall, which suppresses the development of instability waves at low Reynolds numbers. With the increase in θ_{in}, the free shear layer shifts toward the axis and eventually becomes unstable. In the presence of centrifugal and Coriolis forces, the instabilities involved in the swirling flow are not simply Kelvin-Helmholtz instabilities. Gallaire and Chomaz[22] summarized four types of instabilities in total: axial Kelvin-Helmholtz instabilities, azimuthal Kelvin-Helmholtz instabilities, inertial waves, and centrifugal instabilities. The Rayleigh criterion states that the centrifugal instability occurs only if $\partial(ru_\theta)^2/\partial r < 0$.[22] In the present configuration, fluid is injected through an annular entrance on the sidewall and the flow circulation is lower in the center region, so the centrifugal instability does not occur and only the other three kinds of instabilities are possible.

In most previous studies of free shear layers,[10–14] a Stewartson layer was produced by a rotating disk in a container with different rotation speed. One important conclusion of those studies is that the onset of the instability waves and the transition between different wave modes are determined by the Reynolds number based on the azimuthal velocity difference across the free shear layer and the thickness of this layer. In general, a higher Reynolds number leads to a lower wave number. However, in our model, the radius and thickness of the circular free shear layer, as well as the difference of azimuthal velocity across the layer, are implicitly dependent on the injection angle θ_{in} and Reynolds number Re_θ and can hardly be quantified. In this section, our focus will be on the analysis of the flow patterns induced by instability waves and the dependence of mode selection on those parameters.

In the present configuration, when injection angle θ_{in} increases above a critical value, the flow becomes unstable, and the circular free shear layer rolls up spontaneously into a number of discrete vortices aligned evenly along the perimeter of shear layer. The number of vortices is denoted by an integral number m, and the instability mode is identified by azimuthal wave number m. For each flow, only the most unstable wave mode, as determined by the undisturbed flow condition, can survive. The numerical simulation predicts the flow evolution with the most unstable wave mode.

Here we use the flow with $m = 4$ at $\theta_{in} = 45°$ and $\mathrm{Re}_\theta = 500$ as an example to discuss the characteristics of the instabilities developed in the free shear layer. An overview of the flow patterns is given in Fig. 12. The patterns of vorticity magnitude shown in Fig. 12(a) illustrate four identical spiral vortex cores created in the upstream region. The vortex cores begin with a longitudinally aligned straight segment and then develop a spiral shape at a small distance from the head end. The shape of the vortex cores implies that the instability waves are initiated by the disturbances in azimuthal velocity near the head end and propagate azimuthally along the circle where the free shear layer is located. In this region, the axial velocity is close to zero. As the injected flow turns downstream, the difference in axial velocity between the outer main flow and the central recirculating flow begins to take effect; this causes the straight vortex cores to bend and gives rise to the longitudinal component of the instability waves. Since the angular velocity of the CRZ is low in the upstream region and the inertial wave does not develop, the instability waves are essentially of the Kelvin-Helmholtz type as the result of the azimuthal and axial velocity differences across the free shear layer. On the cross section x = 0.1, four eye-like vortex cores with concentrated vorticity magnitude can be observed clearly. The contours on

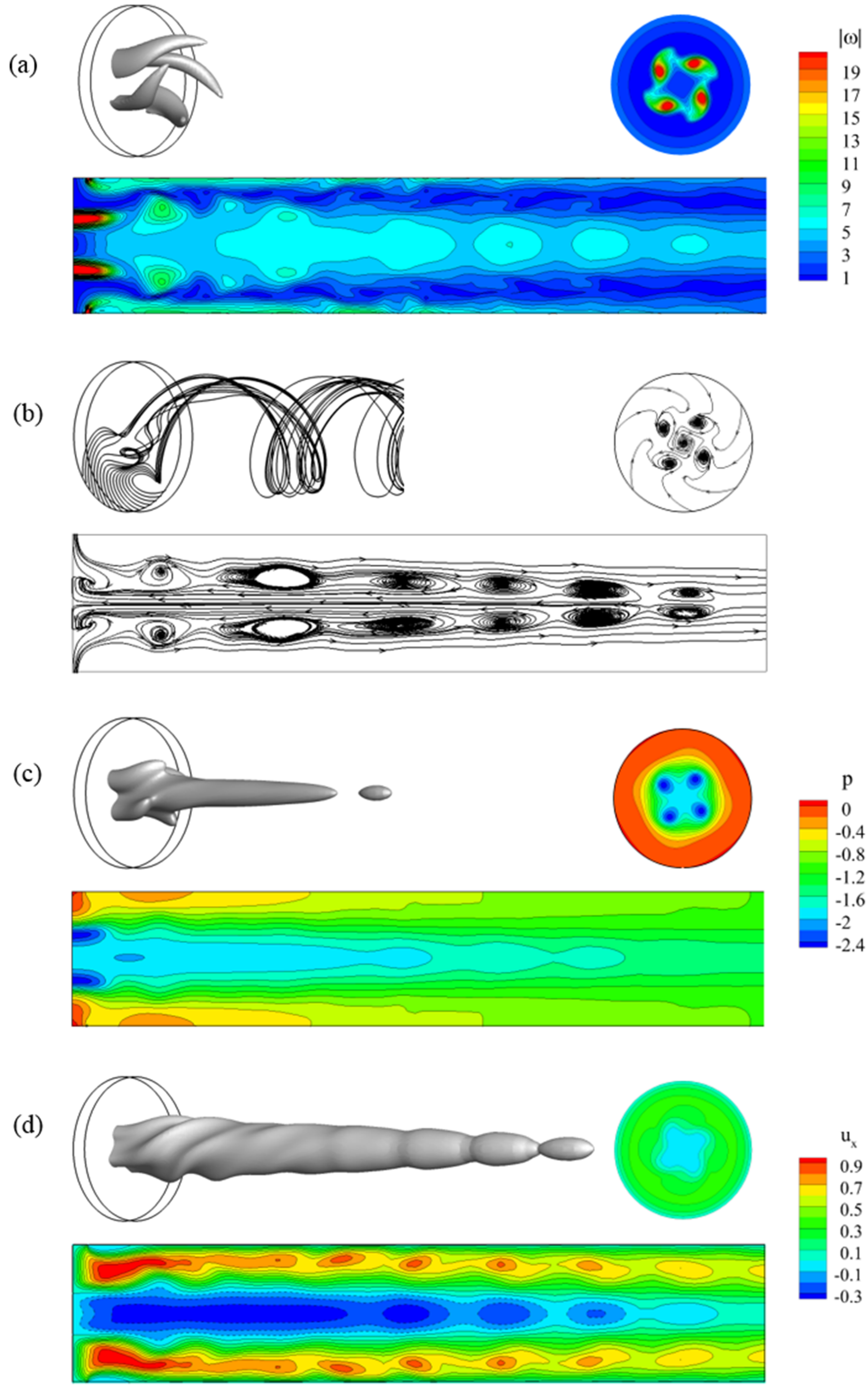

FIG. 12. Patterns of the columnar CRZ with instability waves at θ_{in} = 45° and Re_θ = 500. Contours at cross section x = 0.1 and longitudinal central plane z = 0. (a) Vorticity magnitude, $|\vec{\omega}|_{iso}$ = 10; (b) streamlines; (c) pressure, p_{iso} = −1.85; (d) axial velocity, $(u_x)_{iso} = 0$.

the longitudinal plane show that the strength of the vortex cores decays gradually as flow travels downstream.

Figure 12(b) shows typical three-dimensional streamlines around one vortex core and the projected streamlines on the cross section $x = 0.1$ and the longitudinal central plane $z = 0$. The streamlines are constructed with the velocity components in the frame rotating with the flow structures, so they coincide with the trajectories of fluid particles in the rotating frame. With the development of instability waves, the axisymmetric flow pattern is disturbed. The streamlines around each vortex core rotate about the core axis and travel in small-scale spiral paths along the vortex core in a large-scale spiral shape. On the planes $x = 0.1$ and $z = 0$, the instability waves appear as a series of eye-like recirculating bubbles in the projected streamlines. The "eye" centers represent the points where the vortex cores pass through the planes.

Because of the small-scale rotation of the fluid particles, a number of low-pressure cores are created along the vortex cores, as shown in Fig. 12(c). From the pressure contours on planes $x = 0.1$ and $z = 0$, it can be seen that the pressure magnitude in the low-pressure cores is even lower than on the axis caused by the swirl motion of the bulk flow. Figure 12(d) gives the patterns of axial velocity u_x. The iso-surfaces at $u_x = 0$ show the surfaces of the central flow reversal zone defined as the region in which $u_x < 0$. Because of the instability waves, some corrugations, whose patterns are consistent with the shapes of vortex cores, can be observed on the surfaces. In the u_x contours on the planes $x = 0.1$ and $z = 0$, the flow reversal zone surrounded by a symmetrically deformed outer zone with $u_x > 0$ can be identified on the axis. In this situation, the deformed CRZ may no longer be closed, and mass transfer with the outer flow may take place. This pattern implies that although the flow loses stability, the basic flow structure, in which the flow injected into the chamber travels downstream in the outer region and envelops a CRZ, is preserved.

The surfaces of the central reversal zone, in which $u_x < 0$, are shown in Fig. 12(d). The upstream region is dominated by the Kelvin-Helmholtz waves, which form a spiral pattern on the surfaces of the reversal zone. As the flow goes downstream, the spiral pattern attenuates and transitions to an axisymmetric wavy pattern, which represents a longitudinal wave. The reason for this attenuation and change in shape is that in the course of flow traveling downstream, the flow shear is weakened through viscous diffusion and dissipation, and this inhibits the portion of the waves related to Kelvin-Helmholtz instabilities in the azimuthal and axial directions. We have shown in Fig. 5 that the central recirculating flow takes on a solid-body rotation, and the rotation speed increases gradually as the flow travels downstream. The inertial waves are triggered when the rotation speed meets the criterion for the development of inertial waves. As a result, the downstream flow is dominated by longitudinally propagating inertial waves.

So far, we have identified three different kinds of instability waves: azimuthally and longitudinally propagating Kelvin-Helmholtz waves, and inertial waves. All these waves appear simultaneously and interact with each other, making it difficult to determine the features of each individual wave. Spatial averaging in the azimuthal direction can help us to separate the azimuthally propagating waves from their longitudinal counterpart. Figure 13 presents the flow patterns based on the azimuthally averaged flow field. The azimuthally averaged velocities are denoted by $\langle u \rangle_\theta$. The longitudinally aligned recirculation bubbles shown by the streamlines in Fig. 13(a), as well as the modulated patterns in the contours of axial and swirl velocities in Figs. 13(b) and 13(c), clearly demonstrate the development of the longitudinally propagating waves. The streamline patterns indicate that in the upstream region small bubbles deviate from the axis and align roughly in the layer where the free shear layer is located. The bubbles gradually converge to the axis as the flow travels downstream. The longitudinal waves include not only the inertial waves caused by the solid-body rotation of the central recirculating flow in the downstream region but also the longitudinally propagating Kelvin-Helmholtz instability

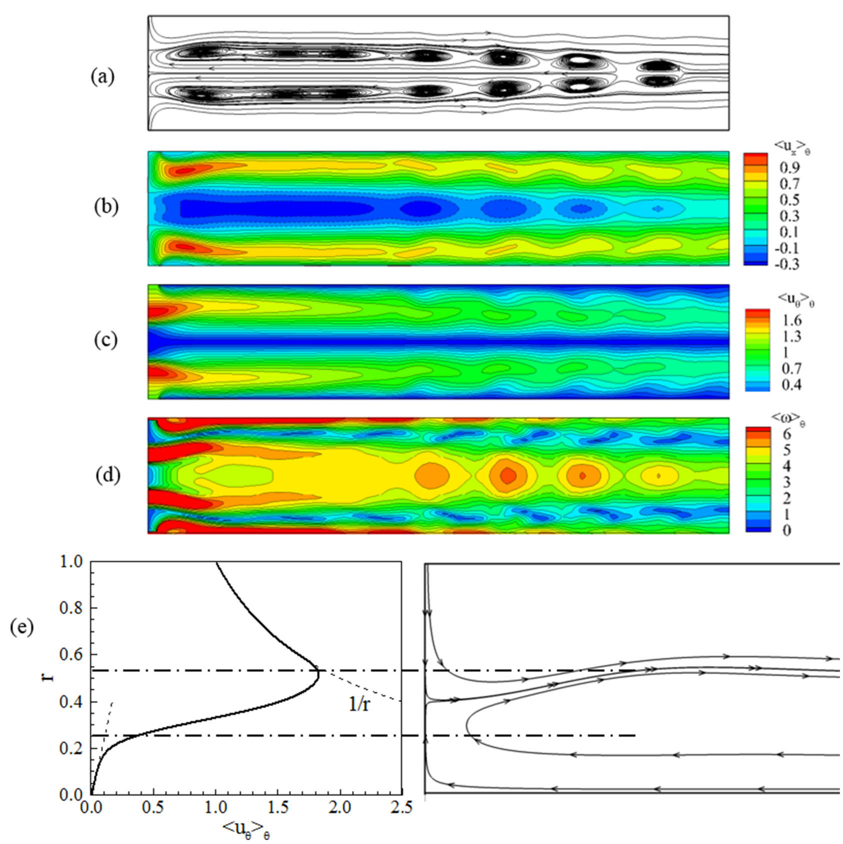

FIG. 13. Flow patterns based on the azimuthally averaged flow field at $\theta_{in} = 45°$ and $\mathrm{Re}_\theta = 500$. (a) Projected streamlines on the x-y plane; (b) contours of axial velocity $\langle u_x \rangle_\theta$ on the x-y plane; (c) contours of azimuthal velocity $\langle u_\theta \rangle_\theta$ on the x-y plane; (d) contours of vorticity magnitude of the azimuthally averaged flow field; (e) profile of azimuthal velocity on the slip head end.

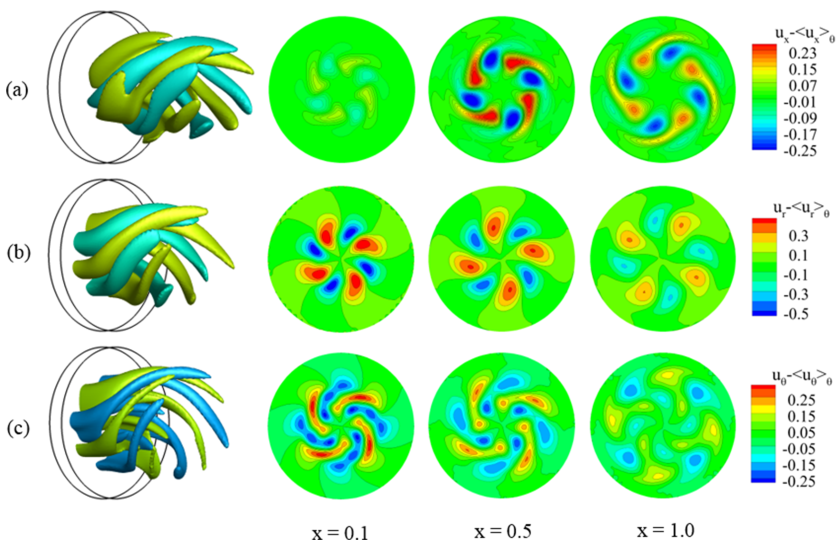

FIG. 14. Patterns of perturbation velocity components at $\theta_{in} = 45°$ and $\mathrm{Re}_\theta = 500$. Left column: iso-surfaces of perturbation velocity components; right three columns: contours of perturbation velocity components at cross sections x = 0.1, 0.5, and 1.0. (a) $u_x - \langle u_x \rangle_\theta$; (b) $u_r - \langle u_r \rangle_\theta$; (c) $u_\theta - \langle u_\theta \rangle_\theta$.

waves developing in the free shear layer. As discussed with respect to Figs. 3 and 5, in the upstream region, the free shear layer is stronger and the central flow rotates more slowly, so the flow is dominated by Kelvin-Helmholtz instabilities. In the downstream region, the flow shear due to axial velocity difference has been mostly dissipated and the central flow rotates faster. These two issues cause the transition from Kelvin-Helmholtz waves to inertial waves in the downstream region.

The contours of vorticity magnitude based on the azimuthally averaged flow field are shown in Fig. 13(d). In the upstream region, the free shear layer, which contributes to the longitudinally propagating Kelvin-Helmholtz waves, can be clearly identified. In the downstream region, a series of oval blocks with higher vorticity magnitude are aligned periodically on the axis. The convergence of vorticity in the ovals is caused by the flow recirculation of inertial waves. Figure 13(e) shows the distribution of the azimuthally averaged azimuthal velocity on the slip head end. The azimuthal velocity of the outer flow above the free shear layer obeys the conservation of angular momentum, and the central recirculating flow continues in solid-body rotation. The free shear layer based on the azimuthally averaged flow field is thicker than that of the axisymmetric base flow under the same conditions before the instabilities occur.

The patterns of the perturbation velocity components u_x', u_r', and u_θ' are shown in Fig. 14. The perturbation velocities are obtained by subtracting the azimuthally averaged velocities from the instantaneous velocities, $u' = u - \langle u \rangle_\theta$. The contours on cross sections $x = 0.1$, 0.5, and 1.0 are compared. For the present geometry, the entrance width is $d = 0.2$, so the cross section $x = 0.1$ is at the halfway point of the entrance, and the other two are downstream. Figure 14(a) shows clearly that the magnitude of u_x' at $x = 0.5$ and 1.0 is larger than that at $x = 0.1$. This is because that the injected flow has not fully developed at $x = 0.1$. With the development of azimuthal waves near the entrance, however, u_r' and u_θ' grow from the slip head end and decay further downstream, as shown in Figs. 14(b) and 14(c).

In order to find the temporal characteristics of the instability waves, we place probes in the flow to record the time variations of the flow variables. Figure 15 shows the positions of the probes and the variations of axial velocity with time at these points. Point 1 is located in the free shear layer, where the azimuthal instability waves develop. Points 2 and 3 are on the axis in the upstream region and can be used to record flow variation due to longitudinally propagating Kelvin-Helmholtz instability waves. Points 4, 5, and 6 are on the axis in the downstream region to record flow variation due to inertial waves. Periodic variations of axial velocity are clearly observed at these points. The wave frequency at probe 1 is much higher than that at the other points. However, under the current conditions, the flow in the upstream region is dominated by azimuthal wave m = 4, so the wave frequency is four times the frequency given by the other probes. At points 2-6, the curves demonstrate an approximately uniform frequency, which means that although the longitudinal

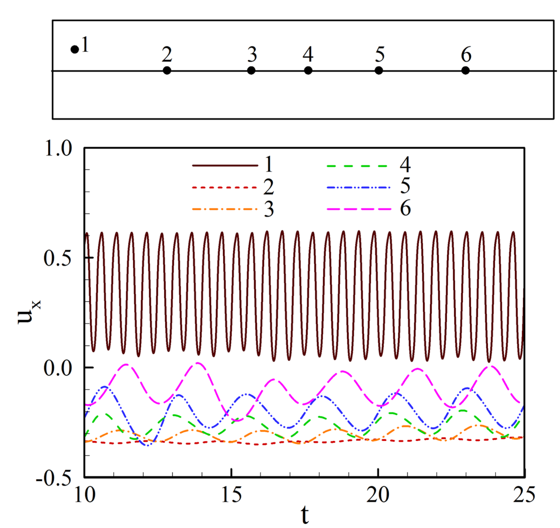

FIG. 15. Temporal variations of axial velocity at different points in the flow field at $\theta_{in} = 45°$ and $\mathrm{Re}_\theta = 500$.

waves in the upstream and downstream regions are of different types, the interaction between them unifies the wave frequency. In our simulation, the frequencies of the azimuthal and longitudinal waves are fairly close—$f_\theta = 0.482$ and $f_x = 0.434$, respectively.

The onset of instabilities and mode selection of the azimuthal waves are determined by the injection angle and Reynolds number. The former has two effects. First, the radius of the circular free shear depends on the injection angle. A higher injection angle gives a larger radial component of injection velocity, which pushes the free shear layer closer to the axis. A decrease in the perimeter of the free shear layer will lead to a reduction of the azimuthal wave number. Second, the azimuthal velocities on both sides of the free shear layer are determined by the injection angle. In the flow outside the free shear layer, the azimuthal velocity satisfies the conservation of angular momentum. As a result, the azimuthal velocity at the outer border of the free shear layer is inversely proportional to the radial coordinate, and a higher injection angle will result in an increase in the azimuthal velocity at the outer border of the free shear layer. Correspondingly, the speed of the solid-body rotation of the central recirculating flow increases. The immediate consequence of the increased solid-body rotation speed is that the Coriolis force effect is strengthened, and the inertial waves develop more easily. For this reason, the flows at higher injection angles are more complex. In the present study, the chamber radius is used as the characteristic length to define the Reynolds number (note that some studies use the thickness of the free shear layer[11–14]). The influence of the Reynolds number lies in the thickness of the free shear layer and the dissipation rates of flow shear strength and swirl concentration. A higher Reynolds number leads to a thinner shear layer, which facilitates the transition from a lower wave number to a higher wave number. The trend is therefore different from those of the previous studies.

Figures 16 and 17 summarize the dependence of the azimuthal wave mode on the injection angle and Reynolds number, as shown by the vorticity magnitude. Except for the flows at low injection angles and high Reynolds numbers, which will be discussed in Sec. IV C, these two figures cover fairly broad ranges of injection angles (30°–75°) and Reynolds numbers (200–2000) and include almost all the wave modes appearing in the laminar flow regime.

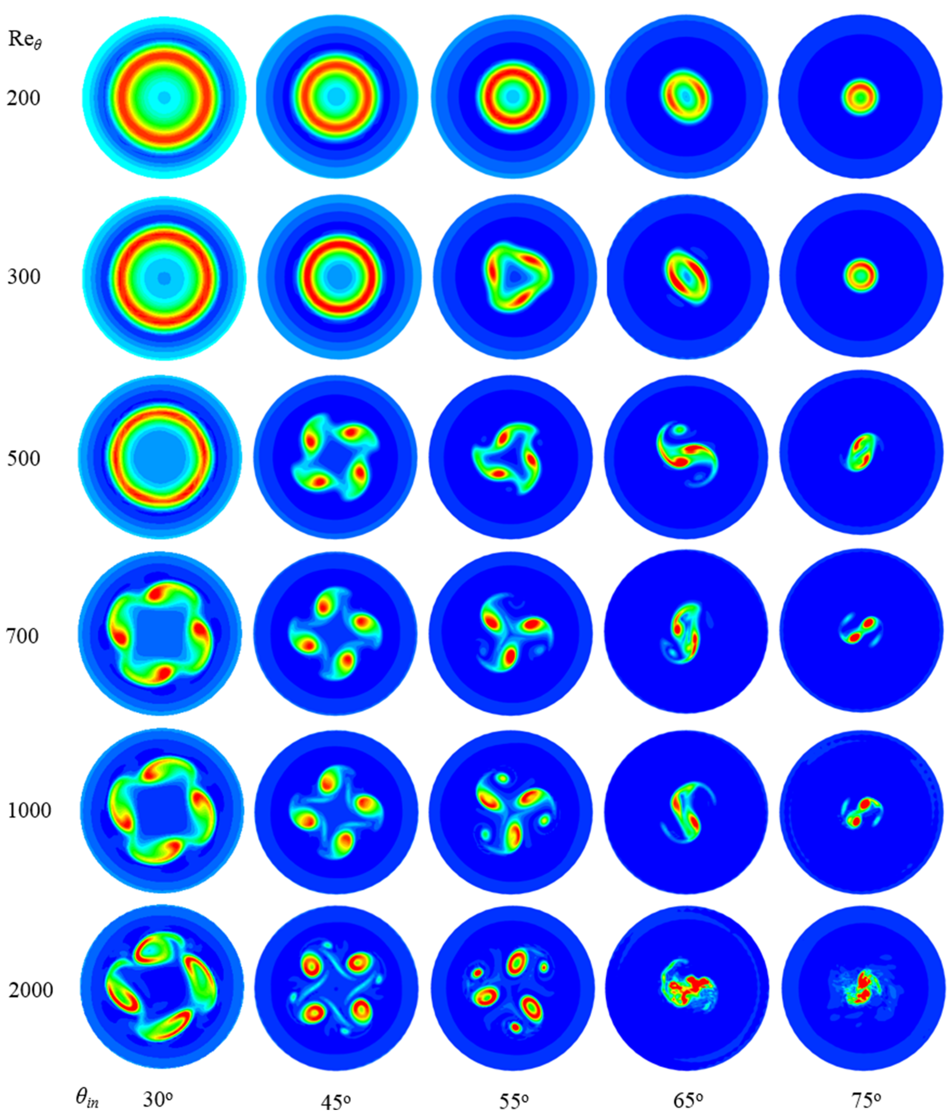

FIG. 16. Contours of vorticity magnitude at x = 0.1 for the columnar CRZ with instability waves at different Reynolds numbers and injection angles. Color scale is different for each figure.

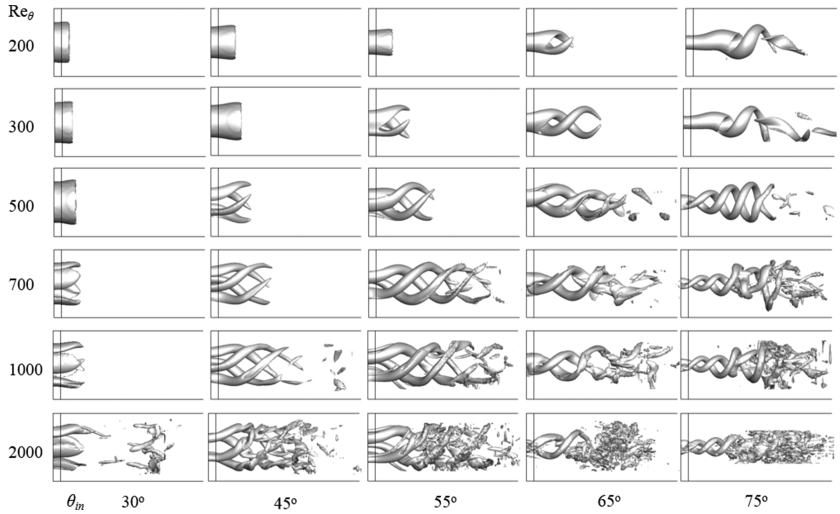

FIG. 17. Iso-surfaces of vorticity magnitude for the columnar CRZ with instability waves at different Reynolds numbers and injection angles. The iso-surface level is different for each figure.

Figure 16 shows the contours of vorticity magnitude at cross section x = 0.1. They are organized by the Reynolds number (rows) and injection angle (columns). To show the vortex patterns clearly, the color scales are different for every figure. The circular ring patterns at low Reynolds numbers and low injection angles show the axisymmetric free shear layer in the basic flow without instability waves. The occurrence and behavior of the instability waves in the free shear layer are determined by both the injection angle and Reynolds number.

At any given injection angle θ_{in}, the basic flow becomes unstable at a critical Reynolds number Re_c. For example, at θ_{in} = 30°, the circular free shear layer breaks up into mode $m = 4$ at $\mathrm{Re}_\theta > \mathrm{Re}_c$, where Re_c is between 500 and 700. The critical Reynolds number decreases with the increase in injection angle. As θ_{in} increases up to 65°, the critical Reynolds number decreases below 200. The higher injection angle makes the flow more prone to lose stability. After the instabilities arise, the wave mode does not show strong dependence on the Reynolds number in the range of Re considered in this study. The exception to this trend appears at θ_{in} = 75°. In this case, as the Reynolds number increases from 300 to 500, the mode number increases from 1 to 2. In our simulations with θ_{in} < 75°, this kind of mode transition caused by the Reynolds number was not observed. The vortex patterns are more complex at higher Re_θ. θ_{in} = 45° and θ_{in} = 55°; when Re increases from 700 to 2000, the solid vortex cores expand and roll up and finally evolve into a hollow tabular structure. At θ_{in} = 65° and 75°, the injection angle is so high that the instability waves are squeezed to the center region and rotate at high speed. At Re_θ = 2000, the smooth vortex structures are lost and the small-scale chaotic disturbances appear. The flow has entered the turbulent state. Comparison of these patterns confirms that the injection angle influences the wave mode by varying the perimeter of the free shear layer and the azimuthal velocity in the layer. When the injection angle increases from 30° to 75°, the perimeter of the circle along which the vortex cores move decreases, and the wave number decreases from m = 4 to 2. At the same time, with an increase in azimuthal velocity, the flow becomes more and more chaotic. In the range of parameters considered in this study, the injection angle plays a more important role than the Reynolds number in determining the wave mode.

The corresponding three-dimensional iso-surfaces of vorticity magnitude at different injection angles and Reynolds numbers are shown in Fig. 17. With the aim of demonstrating the vortex topologies, the levels of the iso-surfaces are adjusted to an appropriate value for each flow; the levels are different for each case. At a lower Reynolds number ($\mathrm{Re}_\theta \leq 1000$), the vortex cores stay smooth and clean. At Re_θ = 2000, the smooth vortex structures burst into fine structures when the flow travels about one-chamber-diameter length downstream, but the large scale spiral patterns of the fine structures can still be identified.

The injection angle and Reynolds number also influence the behaviors of the longitudinal waves. Generally, the increase in Reynolds number makes the free shear layer unstable and facilitates the development of longitudinal Kelvin-Helmholtz instability waves. On the other hand, the increase in injection angle not only decreases the radius of the CRZ but also increases the rotation speed of the CRZ. Both promote the development of longitudinal inertial waves.

C. Columnar central recirculation zone with instability waves at high swirl level and high Reynolds number

For a flow with a low injection angle, that is, high swirl level, the sidewall suppresses the instability waves and the flow remains axisymmetric when the Reynolds number is not large enough. When Re_θ goes beyond a critical point, the flow becomes unstable and instability waves develop. This kind of instability wave is different from those discussed in Sec. IV B, and the mechanisms are more complicated.

Figure 18 shows the instantaneous flow patterns of the instability waves at θ_{in} = 20° and Re_θ = 1000. The free shear layer breaks up into six or seven discrete vortex cores, which are aligned on the edges of a triangle on the head end. Even after an extended long computational time, the flow does not reach a quasi-steady state. The vortex cores shift irregularly on the triangle at a relatively low speed, and the shape of each

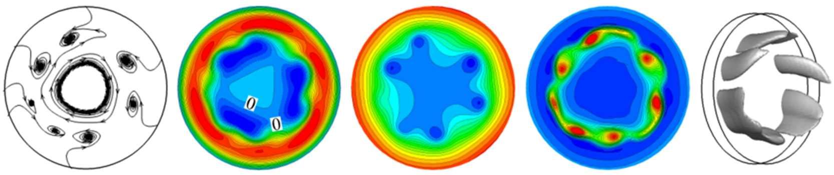

FIG. 18. Flow patterns of instability waves at high swirl level (θ_{in} = 20° and Re_θ = 1000). Cross section at x = 0.1. (a) Projected streamlines; (b) contours of axial velocity; (c) contours of pressure; (d) contours of vorticity magnitude; (e) iso-surfaces of vorticity magnitude.

vortex core changes with time. The large-scale triangle on which the vortex cores are located rotates about the axis at a fairly constant speed. Comparing with the instability waves discussed in Sec. IV B, it is apparent that the Kelvin-Helmholtz instability waves developing in the free shear layer are influenced by other effects at high swirl levels and high Reynolds numbers.

The azimuthally averaged flow patterns are given in Fig. 19. Unlike at low swirl level, neither the projected streamlines nor the contours of axial and azimuthal velocities show any obvious longitudinal waves. The streamlines are only slightly disturbed downstream. One major difference, however, is that the upstream traveling flow in the CRZ deviates from the axis near the head end and creates a smaller CRZ with the opposite recirculation direction. We have shown in Sec. IV A that the CRZ rotates faster in the downstream region. As the flow in the CRZ travels back to the upstream region, the decrease in azimuthal velocity generates a negative pressure gradient on the axis, which forces the flow to deviate from the axis and creates a recirculation zone when the Reynolds number is high enough. In our simulations, the smaller CRZ appears at about Re_θ = 900. The critical value also depends, however, on the injection angle. The profile of azimuthal velocity on the slip head end shown in Fig. 19(d) indicates that the smaller recirculation zone takes on a solid-body rotation. It is very likely that the triangular distribution of the vortex cores shown in Fig. 18 is caused by the generation of the smaller CRZ, but at present, we have no proof supporting this hypothesis.

The distributions of perturbation velocity components $u' = u - \langle u \rangle_\theta$ at different cross sections are given in Fig. 20. These contours clearly show that in the upstream region (x = 0.1, 0.5 and 1.0) m = 6 is the dominant wave mode in the outer layer, but in the central region, m = 3 is dominant. In the downstream region (x = 2.0), only the m = 3 mode can be observed. According to the dependence of the wave mode on the injection angle shown in Figs. 16 and 17, it is reasonable for the instability waves to be dominated by m = 6 in the outer region at θ_{in} = 20°. In the central and downstream regions, although the mechanisms are as yet unidentified, the m = 3 mode becomes dominant.

Figure 21 shows comparisons of vortex patterns at θ_{in} = 10° and 20° with Reynolds numbers ranging from 700 to 3000. The radius of the free shear layer is larger at θ_{in} = 10° than at θ_{in} = 20°. At θ_{in} = 10°, when Re_θ increases from 1000 to 1500, the axisymmetric circular shear layer breaks up into eight identical vortex cores distributed uniformly on the periphery of a circle. When Re_θ increases to

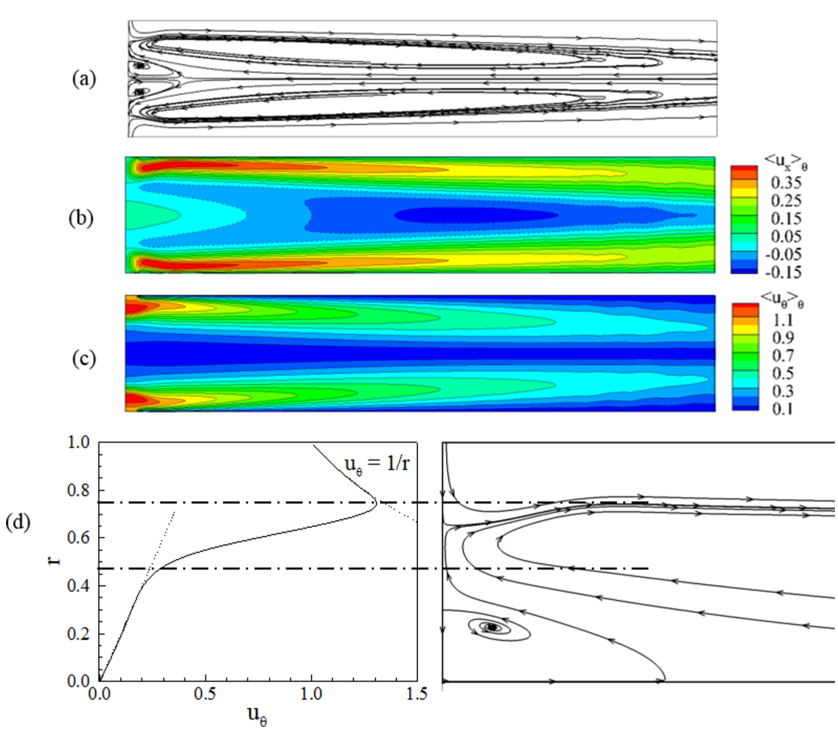

FIG. 19. Flow patterns based on the azimuthally averaged flow field at θ_{in} = 20° and Re_θ = 1000. (a) Projected streamlines on the x-y plane; (b) contours of axial velocity $\langle u_x \rangle_\theta$ on the x-y plane; (c) contours of azimuthal velocity $\langle u_\theta \rangle_\theta$ on the x-y plane; (d) profile of azimuthal velocity on the slip head end.

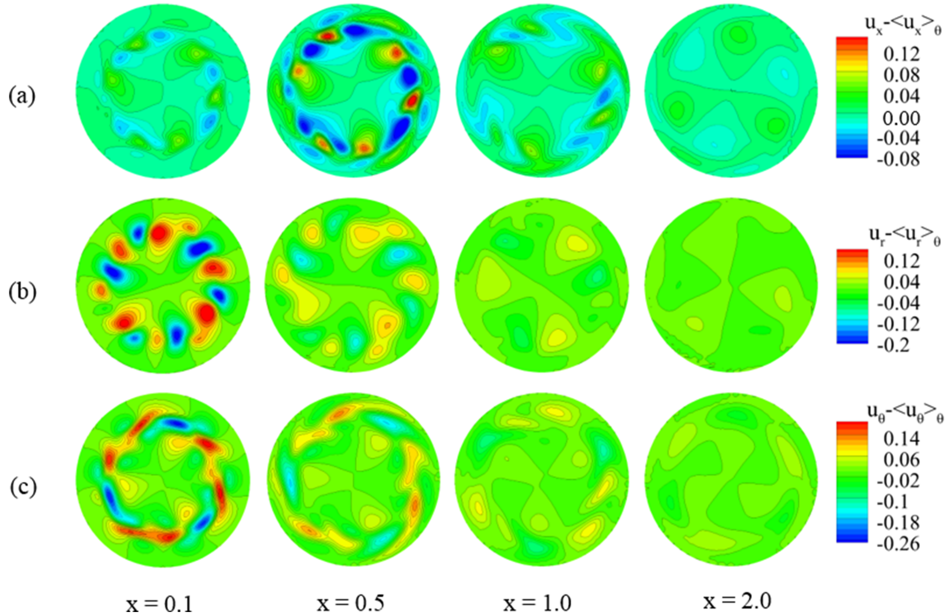

FIG. 20. Patterns of perturbation velocity components in a cylinder with the slip head end at θ_{in} = 20° and Re_θ = 1000. (a) $u_x - \langle u_x \rangle_\theta$; (b) $u_r - \langle u_r \rangle_\theta$; (c) $u_\theta - \langle u_\theta \rangle_\theta$.

2000 and above, these vortex cores are sheared into tapes and rearranged along the edges of a pentagon. The pentagon rotates about the axis with a constant speed, and the shapes of the vortex cores change with time in a random manner. At θ_{in} = 20°, the free shear layer breaks up into six vortex cores at about Re_θ = 700. Further increase in Re_θ results in the alignment of the vortex cores along the edges of a triangle. It is apparent that the edge number of the polygon, the wave mode in the central region, decreases with the increase in injection angle.

D. Summary of flow states and regime diagram

So far, we have identified three types of flow patterns, that is, the flow with an axisymmetric central recirculating zone, the flow with symmetric instability waves in the free shear layer enclosing the CRZ, and the flow with asymmetric instability waves aligned along the edges of a polygon. The occurrence of each kind of the flow pattern is determined by the injection angle θ_{in} and Reynolds number Re_θ.

Figure 22 shows the profiles of azimuthal velocity on the slip head end of all the cases considered in this study. The solid curves represent the cases with basic flows in which an axisymmetric CRZ is created, and the dashed curves are for the cases in which instability waves developed. The dashed curves are based on the azimuthally averaged flow field. This figure demonstrates some important facts. The radius of the free shear layer is primarily determined by the injection angle, and a higher injection angle leads to a smaller radius of the free shear layer. In the outer main flow, the angular momentum is well conserved, and the azimuthal velocity is described by the inverse of the radial coordinate. Inside the free shear layer, the central flow takes on the solid-body rotation. The angular velocity of the central zone increases with an increase in injection angle and decreases with an increase in Reynolds number. The outer and central flows are connected by the free shear layer, which is characterized by a sharp change in azimuthal velocity. In basic axisymmetric flows, the thickness of the free shear layer decreases with an increase in Reynolds number. For flows with instability waves, however, the profiles of azimuthally averaged azimuthal velocity can hardly give an accurate estimation of the thickness of the free shear layer. At the same time, other uncertainties are involved at high injection angles and high Reynolds numbers. These issues mean that the free shear layer thickness cannot be measured accurately.

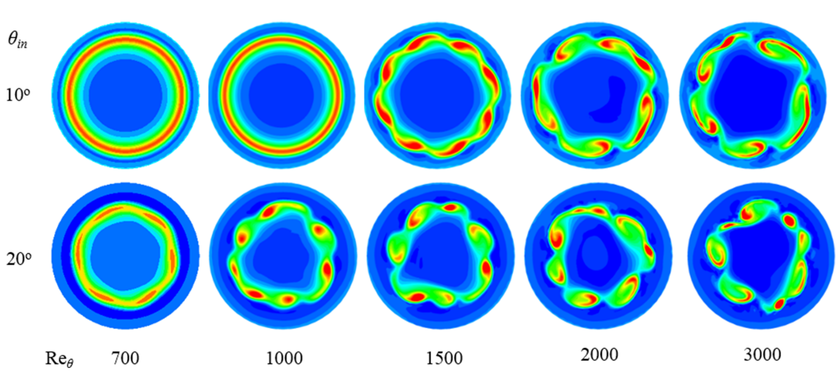

FIG. 21. Contours of vorticity magnitude at x = 0.1 for flow instability at a high swirl level. The color scale is different for each figure.

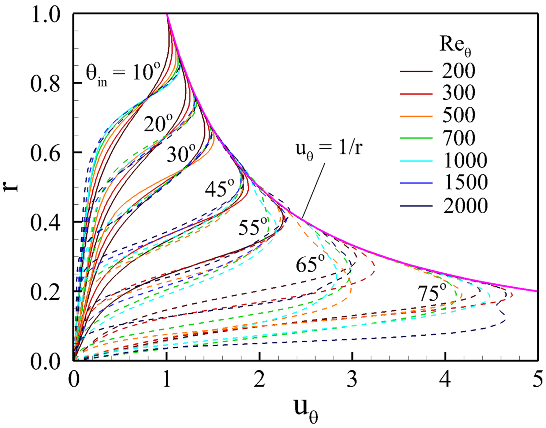

FIG. 22. Profiles of azimuthal velocity on the slip head end at different θ_{in} and Re_θ. Dashed curves based on the azimuthally averaged flow field for cases with instability waves.

The injection angle θ_{in} plays an important role in determining the spatial and temporal features of the instability waves on the surface of the CRZ. Figure 23 shows the variation of the radius of the azimuthal wave train on the head end with the injection angle and the variation of temporal periods of the azimuthal and axial waves with the radius of the azimuthal wave train and the injection angle. (The radius of the azimuthal wave train is also the radius of the CRZ of the azimuthally averaged flow, so it is denoted with $\mathrm{R_{CRZ}}$.) The Reynolds number ranges from 200 to 2000. In this figure, the subscript θ indicates the variables related to the azimuthal waves, and subscript x indicates the variables related to the longitudinal waves.

Figures 23(a) and 23(b) show the dependence of R_{CRZ} on θ_{in} at different Reynolds numbers. In Fig. 23(a), the vertical coordinate $\mathrm{R_{CRZ}}$ is in logarithmic scale, and the horizontal coordinate θ_{in} is in linear scale. In Fig. 23(b), the horizontal coordinate θ_{in} is logarithmic scale, and the vertical coordinate R_{CRZ} is linear scale. The numerical results are represented by open symbols. The Reynolds number Re_θ does not appear to exhibit influence on R_{CRZ} in the range considered in this study. The variation of R_{CRZ} suggests that the dependence of R_{CRZ} on θ_{in} separates into two regimes according to the level of θ_{in}. When $\theta_{in} < 45°$, a roughly linear relationship is observed between $\log(R_{CRZ})$ and θ_{in}, yet when $\theta_{in} > 45°$, a roughly linear relationship appears between $\mathrm{R_{CRZ}}$ and $\log(\theta_{in})$. The relationship can be expressed in the form

$$\log R_{CRZ} = a\theta_{in} + b \qquad \theta_{in} < 45°, \tag{14}$$

$$R_{CRZ} = c \log \theta_{in} + d \qquad \theta_{in} > 45°. \tag{15}$$

Taking into account the restrictions $R_{CRZ} = R = 1$ at $\theta_{in} = 0°$ and $R_{CRZ} = 0$ at $\theta_{in} = 90°$, we develop two log-linear correlations between R_{CRZ} and θ_{in} for the present configuration, using the least square method,

$$\log R_{CRZ} = -0.023 \cdot \theta_{in} \qquad \theta_{in} < 45°, \tag{16}$$

$$R_{CRZ} = -0.530 \cdot (\log \theta_{in} - \log 90) \qquad \theta_{in} > 45°. \tag{17}$$

In Fig. 23(c), the temporal periods of the azimuthal and longitudinal waves (T_θ and T_x) versus the radius of the azimuthal wave train R_{CRZ} at $x = 0$ are examined. The numerical results are represented by open symbols for azimuthal waves and solid symbols for longitudinal waves. Just as R_{CRZ} versus θ_{in}, T_θ, and T_x are not much influenced by the Reynolds

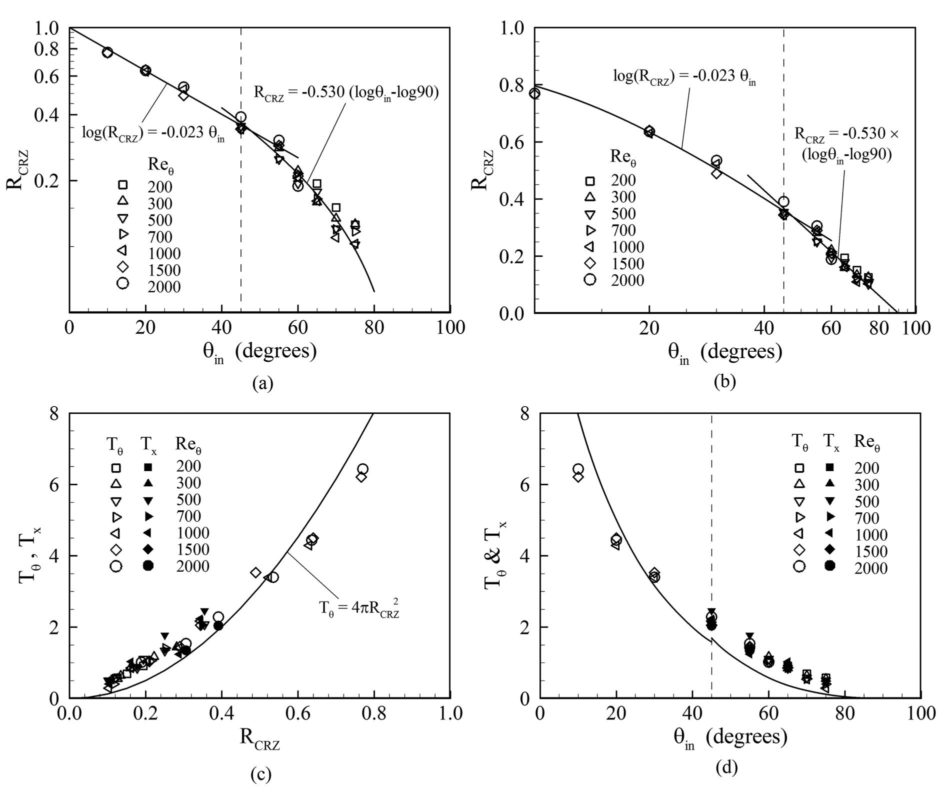

FIG. 23. Temporal and spatial features of azimuthal and longitudinal waves. (a) Radius of azimuthal wave trains on head end versus injection angle, $\mathrm{R_{CRZ}}$ (vertical coordinate) in logarithm scale; (b) radius of azimuthal wave trains on head end versus injection angle, θ_{in} (horizontal coordinate) in logarithm scale; (c) time periods of azimuthal and longitudinal waves versus radius of azimuthal wave train; (d) time periods of azimuthal and longitudinal waves versus injection angle θ_{in}.

number. For each individual case, the period of the azimuthal waves T_θ is almost identical to that of the longitudinal waves T_x, as a result of the interaction between the two types of waves. The azimuthal wave is primarily caused by the Kelvin-Helmholtz instability due to the velocity difference. Its period can be roughly estimated by ignoring the thickness of the free shear layer and the velocity of the central flow,

$$T_\theta = \frac{2\pi R_{CRZ}}{U_{wave}}. \tag{18}$$

The wave velocity is taken to be the average velocity of the outer flow and the central flow,

$$U_{wave} = \frac{1}{2}\left(U_{out} + U_{ctr}\right) \approx \frac{1}{2}\left(\frac{U_{\theta,in}R}{R_{CRZ}} + 0\right). \tag{19}$$

In the nondimensional form, $U_{\theta,in} = R = 1$. Substitution of Eq. (19) into Eq. (18) gives the relationship between T_θ and R_{CRZ},

$$T_\theta = 4\pi R_{CRZ}^2. \tag{20}$$

The period of the azimuthal wave estimated by this model is represented by the solid curve in the figure. The model prediction agrees largely well with the numerical result shown by the open and solid symbols. The discrepancy at larger R_{CRZ} (>0.4) can be attributed to the neglect of the azimuthal velocity of the central recirculating flow, which makes the azimuthal wave speed smaller and the temporal period larger. At smaller R_{CRZ} (<0.4), the neglect of the free shear layer thickness takes effect, which makes the azimuthal wave speed of the model prediction larger and the temporal period smaller.

The dependence of T_θ and T_x on θ_{in} is shown in Fig. 23(d). Using the correlations between R_{CRZ} and θ_{in} given by Eqs. (14)–(17), and the simplified model for T_θ and R_{CRZ} given by Eq. (20), the relationship between the wave period and injection angle can be established analytically, as shown by solid curves in the figure.

Figure 24 gives a regime diagram summarizing the flow states in the space of θ_{in} and Re_θ. In this diagram, "◯" stands for the basic stable state without instability waves. The uncircled numbers represent the state in which the free shear layer breaks up into discrete vortex cores with instability waves, where the number indicates the wave mode. The circled numbers describe the state in which the discrete vortex cores are rearranged and aligned along the edges of a polygon, indicating the number of edges of the polygon. Several observations are noted. For each injection angle, the flow is characterized by a basic axisymmetric pattern ("◯") at lower Reynolds numbers. When the Reynolds number increases beyond a critical value, instability waves develop in the free shear layer. The critical Reynolds number decreases with increasing injection angle, that is, higher injection angles make it is easier for the flow to become unstable to disturbances. On the other hand, a critical injection angle exists for each Reynolds number for the generation of flow instabilities. The increase in injection angle leads to a decrease in the perimeter of the free shear layer. As a result, the mode number decreases. In the range of parameters considered in this study, the Reynolds number is not the major factor influencing wave mode selection. The Reynolds number effect only occurs at $\theta_{in} = 75°$, where the wave mode increases from 1 to 2 when Re_θ increases from 300 to 500. In addition, at low injection angles, an increase in Reynolds number triggers the redistribution of the vortex cores along the edges of a polygon.

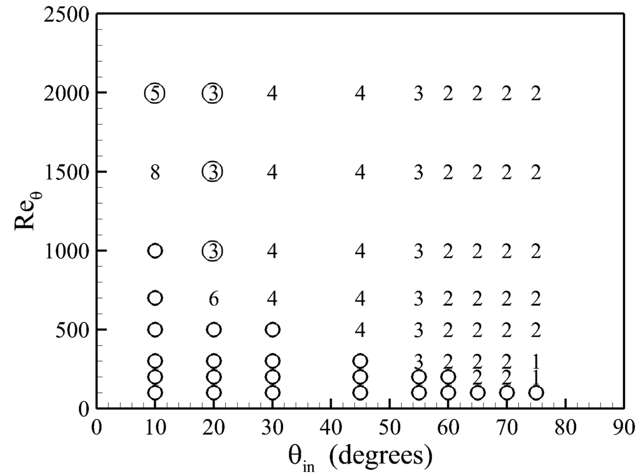

FIG. 24. Diagram of flow regimes. "◯"—basic flow without instability waves; uncircled numbers—mode number of instability waves; circled numbers—the number of edges of polygon along which instability waves are aligned.

E. Linear analysis of flow instability

In this section, a linear analysis of the azimuthal shear instability is performed to provide more insight into the occurrence and mode selection of the instability waves. In the present study, the instabilities originate near the head end, where the flow injected into the chamber drives the central flow to swirl through a free shear layer. If the thickness of the free shear layer is ignored, the present flow can be considered as a special case with zero axial velocity of the screened Rankine vortex, with an added plug flow, as investigated by Gallaire and Chomaz.[22] In their work, the effect of azimuthal shear on the stability of azimuthal wave number m was analyzed extensively with asymptotic expansions and numerical computations of the dispersion relation. They found that the azimuthal shear destabilizes the azimuthal wave mode $|m| \geq 2$, and the axial shear and centrifugal instability are active for all m. The azimuthal Kelvin-Helmholtz instability interacts with its counterpart in the axial direction, centrifugal instability due to higher circulation in the central region, and inertial waves due to solid-body rotation of the central flow. The resultant model constitutes the basic mechanisms of instabilities in swirling flows. In the present study, the circulation $\Gamma(=u_\theta 2\pi r)$ of the outer main flow is far greater than that of the central flow in the upstream region. The centrifugal instability thus does not occur. The low azimuthal velocity also prevents the development of inertial waves in the central region. Therefore, the upstream flow is dominated by the Kelvin-Helmholtz instability due to azimuthal shear when the flow loses stability. The centrifugal and Coriolis forces also play a role.[10]

In real flows, the finite thickness of the free shear layer must be taken into account. Experimental studies have shown that the azimuthal wave number m is roughly proportional to the ratio of the circular shear layer diameter to its thickness.[23,24] This is consistent with the mode variation shown in Fig. 16 and the azimuthal velocity profiles shown in Fig. 22.

The instabilities in the present study are triggered by the azimuthal shear near the head end, where the axial velocity has not developed in the flow, so the instabilities reduce to two-dimensionality and only propagate azimuthally in the upstream region. As shown in Fig. 22, the azimuthal velocity profiles of the undisturbed base flow can be simplified as a continuous piecewise distribution illustrated in Fig. 25, where r_0 is the radius of the circular interface between the outer main flow and the central flow, and δ is the thickness of the free shear layer. In the outer main flow, the azimuthal velocity obeys the conservation of angular momentum as $u_\theta = u_{\theta,in}R/r = \Omega_2(r_0 + \delta/2)^2/r$, where $\Omega_2 = u_{\theta,in}R/(r_0 + \delta/2)^2$ is the angular velocity at the outer boundary of the free shear layer. The central recirculating flow takes on solid-body rotation, and the azimuthal velocity varies linearly with the radial coordinate as $u_\theta = \Omega_1 r$, where Ω_1 is the constant angular velocity of the central flow. Across the free shear layer, the azimuthal velocity decreases linearly from the lower boundary of the outer main flow to the upper boundary of the central flow. The undisturbed azimuthal velocity in the upstream region is given as

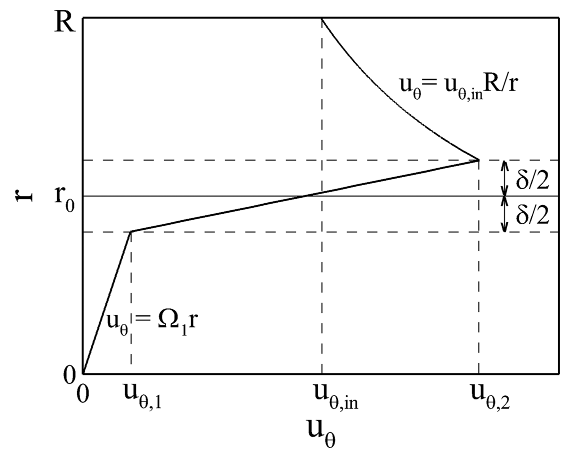

FIG. 25. Simplified piecewise profile of azimuthal velocity.

$$u_\theta = \Omega_2 \frac{(r_0+\delta/2)^2}{r} \qquad (r > r_0 + \delta/2), \tag{21}$$

$$u_\theta = \Omega_1 (r_0 - \delta/2) + \frac{\Omega_2 (r_0+\delta/2) - \Omega_1 (r_0 - \delta/2)}{\delta}[r - (r_0 - \delta/2)] \qquad (r_0 - \delta/2 < r < r_0 + \delta/2), \tag{22}$$

$$u_\theta = \Omega_1 r \qquad (r < r_0 - \delta/2). \tag{23}$$

We seek a solution of perturbation of the type

$$u'_\theta = U_\theta(r)\, e^{i(m\theta/2\pi - \omega t)}, \tag{24}$$

$$u'_r = U_r(r)\, e^{i(m\theta/2\pi - \omega t)}, \tag{25}$$

where $U_\theta(r)$ and $U_r(r)$ are the amplitude of velocity perturbation in the azimuthal and radial directions and ω is the complex wave frequency. The positive imaginary part of ω is a symptom of the unbounded growth of instability. The equivalent wave number in the curvilinear coordinate along the circular central line of the instability wave is

$$k = \frac{m}{2\pi r_0}. \tag{26}$$

Considering the squeezing effect on the equivalent wave number k of the curvature of the circular shear layer, k is modified as

$$k = \frac{m}{2\pi(r_0 - f_{cor}\delta/2)}, \tag{27}$$

where f_{cor} is the correction factor. We choose $f_{cor} = 0.6$ in this analysis.

The present numerical results have shown that in the low Reynolds number range (Re < 1000) the instability is suppressed by the injected flow when the free shear layer is close to the inlet at low injection angles ($\theta_{in} = 10°$ and $20°$). Here, the emphasis is placed on the mechanisms of occurrence and mode selection of instability waves, so we ignore the suppression effect of the injected flow as well as the constraint on the chamber axis and assume that the amplitude of radial velocity perturbation has the following form:

$$U_r = A_+ e^{-k(r-r_0)} \qquad (r > r_0 + \delta/2), \tag{28}$$

$$U_r = A_0 e^{-k(r-r_0)} + B_0 e^{+k(r-r_0)} \qquad (r_0 - \delta/2 < r < r_0 + \delta/2), \tag{29}$$

$$U_r = B_- e^{+k(r-r_0)} \qquad (r < r_0 - \delta/2). \tag{30}$$

At the outer and inner boundaries of the free shear layer, the continuity of U_r is satisfied, so we have

$$A_+ e^{-k\delta/2} = A_0 e^{-k\delta/2} + B_0 e^{+k\delta/2}, \tag{31}$$

$$B_- e^{-k\delta/2} = A_0 e^{+k\delta/2} + B_0 e^{-k\delta/2}. \tag{32}$$

For a simple analysis, we ignore the centrifugal effect and the curvature of the shear layer and utilize the continuous relation for the rectilinear wave proposed by Chandrasekhar[25] at the outer and inner boundaries of the circular free shear layer,

$$-\frac{A_0}{B_0} e^{-k\delta} = \frac{\dfrac{\Omega_2(r_0+\delta/2) - \Omega_1(r_0-\delta/2)}{\delta} + \Omega_2 - 2[\omega + k\Omega_2(r_0+\delta/2)]}{\dfrac{\Omega_2(r_0+\delta/2) - \Omega_1(r_0-\delta/2)}{\delta} + \Omega_2}, \tag{33}$$

$$-\frac{B_0}{A_0}e^{-k\delta} = \frac{\dfrac{\Omega_2(r_0+\delta/2)-\Omega_1(r_0-\delta/2)}{\delta} - \Omega_1 + 2\left[\omega + k\Omega_1(r_0-\delta/2)\right]}{\dfrac{\Omega_2(r_0+\delta/2)-\Omega_1(r_0-\delta/2)}{\delta} - \Omega_1}. \tag{34}$$

Eliminating A_0/B_0, we obtain the dispersion relation

$$e^{-2k\delta} = \left\{\frac{\dfrac{\Omega_2(r_0+\delta/2)-\Omega_1(r_0-\delta/2)}{\delta} + \Omega_2 - 2\left[\omega + k\Omega_2(r_0+\delta/2)\right]}{\dfrac{\Omega_2(r_0+\delta/2)-\Omega_1(r_0-\delta/2)}{\delta} + \Omega_2}\right\} \times \left\{\frac{\dfrac{\Omega_2(r_0+\delta/2)-\Omega_1(r_0-\delta/2)}{\delta} - \Omega_1 + 2\left[\omega + k\Omega_1(r_0-\delta/2)\right]}{\dfrac{\Omega_2(r_0+\delta/2)-\Omega_1(r_0-\delta/2)}{\delta} - \Omega_1}\right\}. \tag{35}$$

The wave frequency ω can be obtained by solving this equation for each equivalent wave number $k(=m/2\pi r_0)$. If ω has a positive imaginary component, the flow is unstable. The growth rate of an unstable instability reads as

$$\sigma = \omega_i, \tag{36}$$

where ω_i is the positive imaginary part of ω.

As typical cases, the flows for θ_{in} = 45° and 55° at Re_θ = 500 are considered here. According to the azimuthal velocity profiles of the azimuthally averaged flow field shown in Fig. 22, the parameters of the simplified piecewise base flow are given in Table II. Through Eqs. (35) and (36), the growth rate σ for each unstable azimuthal wave mode m can be acquired. The dependence of σ on m for these two cases is shown in Fig. 26. The maximum σ at integral m (indicated by solid dots in the figure) shows that m = 4 and 3 are the most unstable modes

TABLE II. Parameters of the piecewise azimuthal velocity profile at θ_{in} = 45° and 55° and Re_θ = 500.

θ_{in} (deg)	r_0	d	Ω_1	Ω_2
45	0.34	0.20	0.41	3.43
55	0.28	0.18	0.41	4.73

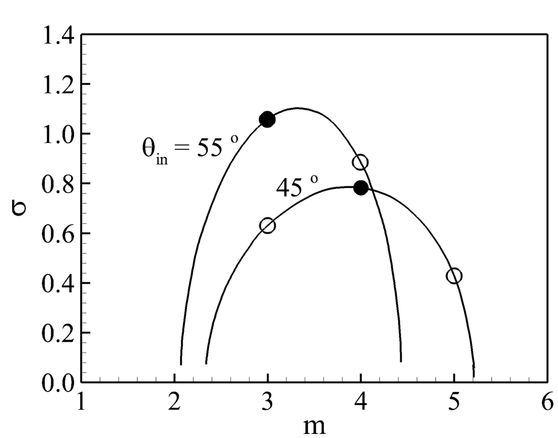

FIG. 26. Growth rate of an instability as a function of azimuthal wave number at θ_{in} = 45° and 55°, and Re_θ = 500. Solid dots indicate the most unstable azimuthal wave mode.

for θ_{in} = 45° and 55°, respectively. This is consistent with the numerical results in terms of mode selection shown in Figs. 16 and 17.

In addition to predicting the most unstable mode, the intrinsic properties of the dispersion relation [Eq. (35)] confirm the observation from the numerical simulation that the wave number m is primarily determined by the radius r_0 and thickness δ of the circular free shear layer, which are functions of injection angle θ_{in} and Reynolds number Re_θ. Due to the limitation of the paper length, a detailed discussion will not be presented here.

As the important nature of instabilities in the swirling flow, the absolute and convective characteristics have been broadly investigated.[26,27] For the simplest inviscid parallel shear flow, Huerre and Monkewitz[28] found that the flow is convectively unstable when the velocity ratio $|U_1 - U_2|/|U_1 + U_2|$ is smaller than a critical value. Otherwise, the flow is absolutely unstable. The flow in the present geometry is much more complex, and analysis of this type is beyond the scope of the present paper. That investigation will be carried out in the future work.

V. CONCLUSIONS

Focusing on instability waves, we attempt to construct a unified theory to connect different flow states over a broad range of flow parameters in the swirling flow. As the first step, we provide a comprehensive analysis of the flow characteristics under different conditions in a cylindrical chamber with a slip head end.

At a high swirl level, that is, at a low injection angle, the flow is characterized by an axisymmetric central recirculation zone. The motion of the central flow is driven by the outer main flow through a free shear layer enclosing the central recirculation zone. The outer flow obeys the conservation of angular momentum, and the central flow takes on a solid-body rotation. The radius of the free shear layer is primarily determined by the injection angle. A higher injection angle pushes the shear layer closer to the axis. Our results confirm that the central recirculation zone only appears when the swirl number exceeds a critical value. We found that the longitudinal dimension of the central recirculation zone is linearly dependent on the Reynolds number and injection angle in logarithm scale, which suggests the expression $L_{CRZ} = c\,\mathrm{Re}_\theta^a\,\theta_{in}^b$ to describe the length. In addition, we found that the logarithm of the swirl number satisfies a segmentally linear relationship with the axial coordinate. In the upstream section of the swirler, with the central recirculation zone, all the curves of the swirl number are collapsed into a single curve with the axial coordinate normalized with L_{CRZ}. These linear relationships clearly demonstrate that the flow with the central recirculation zone is a linear phenomenon, and all the flow behaviors are predictable with simple expressions.

When the injection angle increases up to a certain value, the basic flow loses stability and instability waves develop in the free shear layer and the central flow. In the present study, we identify three kinds of instability waves: azimuthal and longitudinal Kelvin-Helmholtz waves originating in velocity change across the free shear layer and inertial waves from the solid-body rotation of the central flow. In the range of injection angle and Reynolds number considered in this study, the azimuthal wave mode is primarily determined by the injection angle. An increase in injection angle leads to a decrease in the perimeter of the free shear layer, which causes a reduction in mode number. Compared with the injection angle, the Reynolds number plays a minor role in mode selection. The longitudinal waves contain both Kelvin-Helmholtz waves and inertial waves. The Kelvin-Helmholtz waves are dominant in the free shear layer near the head end, whereas the inertial waves are generally dominant in the downstream section of the central recirculation zone, where the azimuthal velocity is sufficiently large. Our results show that the time periods or frequencies of the azimuthal waves are close to those of the longitudinal waves. An exponential relationship between the time periods of the waves and the injection angles is obtained in the simulations.

At a high swirl level and high Reynolds number, discrete vortex cores formed by the instability waves are aligned on the edges of a polygon. It is possible that this is due to the formation of a second central recirculation zone on the axis due to high swirl in the upstream-traveling flow on the axis.

In addition to the numerical simulation, a linear analysis of azimuthal instabilities in the upstream section is carried out, taking into account the variation of azimuthal velocity in the outer main flow and the central recirculating flow, as well as the transition through the free shear layer with finite thickness. The most unstable wave modes predicted by the linear analysis agree well with those from the numerical simulation; the mode selection mechanisms identified through the numerical simulation are confirmed.

ACKNOWLEDGMENTS

This work was sponsored partly by the Air Force Office of Scientific Research under Grant No. FA 9550-10-1-0179 and partly by the William R. T. Oakes Endowment of the Georgia Institute of Technology. The authors gratefully acknowledge support and advice from Mitat A. Birkan.

[1] N. Syred and J. M. Beer, "Combustion in swirling flows: A review," Combust. Flame **23**, 143–201 (1974).
[2] A. K. Gupta, D. G. Lilley, and N. Syred, *Swirl Flows* (Abacus Press, 1984).
[3] Y. Huang and V. Yang, "Dynamics and stability of lean-premixed swirl-stabilized combustion," Prog. Energy Combust. Sci. **35**, 293–364 (2009).
[4] S. W. Wang, S. Y. Hsieh, and V. Yang, "Unsteady flow evolution in swirl injector with radial entry. I. Stationary conditions," Phys. Fluids **17**, 045106 (2005).
[5] S. W. Wang and V. Yang, "Unsteady flow evolution in swirl injectors with radial entry. II. External excitations," Phys. Fluids **17**, 045107 (2005).
[6] X. Chen and V. Yang, "Effect of ambient pressure on liquid swirl injector flow dynamics," Phys. Fluids **26**, 102104 (2014).
[7] X. Wang, H. Huo, Y. Wang, and V. Yang, "Comprehensive study of cryogenic fluid dynamics of swirl injectors at supercritical conditions," AIAA J. **55**, 3109–3119 (2017).
[8] B. T. Vu and F. C. Gouldin, "Flow measurements in a model swirl combustor," AIAA Paper 80-0076, 1980.
[9] R. Hide and C. W. Titman, "Detached shear layers in a rotating fluid," J. Fluid Mech. **29**, 39–60 (1967).
[10] K. Stewartson, "On almost rigid rotations," J. Fluid Mech. **3**, 17–26 (1957).
[11] A. I. Vooren, "The Stewartson layer of a rotating disk of finite radius," J. Eng. Math. **26**, 131–152 (1992).
[12] M. Rabaud and Y. Couder, "A shear-flow instability in a circular geometry," J. Fluid Mech. **136**, 291–319 (1983).
[13] H. Niino and N. Misawa, "An experimental and theoretical study of barotropic instability," J. Atmos. Sci. **41**, 1992–2011 (1984).
[14] J. A. Konijnenberg, A. H. Nielsen, J. Rasmussen, and B. Stenum, "Shear-flow instability in a rotating fluid," J. Fluid Mech. **387**, 177–204 (1999).
[15] W. G. Früh and A. H. Nielsen, "On the origin of time-dependent behaviour in a barotropically unstable shear layer," Nonlinear Processes Geophys. **10**, 289–302 (2003).
[16] S. Poncet and M. P. Chauve, "Shear-layer instability in a rotating system," J. Flow Visualization Image Process. **14**, 85–105 (2007).
[17] B. A. Finlayson and L. E. Scriven, "The method of weighted residuals and its relation to certain variational principles for the analysis of transport processes," Chem. Eng. Sci. **20**, 395–404 (1965).
[18] A. Kovacs and M. Kawahara, "A finite element scheme based on the velocity correction method for the solution of the time-dependent incompressible Navier-Stokes equations," Int. J. Numer. Methods Fluids **13**, 403–423 (1991).
[19] Y. Wang, X. Lu, and L. Zhuang, "Numerical analysis of the rotating viscous flow approaching a solid sphere," Int. J. Numer. Methods Fluids **44**, 905–925 (2004).
[20] Y. Wang, X. Lu, L. Zhuang, Z. Tang, and W. Hu, "Numerical simulation of drop Marangoni migration under microgravity," Acta Astronaut. **54**, 325–335 (2004).
[21] G. K. Batchelor, *An Introduction to Fluid Mechanics* (Cambridge University Press, 1967).
[22] F. Gallaire and J.-M. Chomaz, "Instability mechanisms in swirling flows," Phys. Fluids **15**, 2622–2639 (2003).
[23] G. F. Carnevale and R. C. Kloosterziel, "Emergence and evolution of triangular vortices," J. Fluid Mech. **259**, 305–331 (1994).
[24] K. Bergeron, E. A. Coutsias, J. P. Lynov, and A. H. Nielsen, "Self-organization in circular shear layer," Phys. Scr. **T67**, 33–37 (1996).
[25] S. Chandrasekhar, *Hydrodynamic and Hydromagnetic Stability* (Oxford at The Clarendon Press, 1961).
[26] M. Turkyilmazoglu, J. W. Cole, and J. S. B. Gajjar, "Absolute and convective instabilities in the compressible boundary layer on a rotating disk," Theor. Comput. Fluid Dyn. **14**, 21–37 (1999).
[27] T. Loiseleux, I. Delbende, and P. Huerre, "Absolute and convective instabilities of a swirling jet/wake shear layer," Phys. Fluids **12**, 375–380 (2000).
[28] P. Huerre and P. A. Monkewitz, "Absolute and convective instabilities in free shear layers," J. Fluid Mech. **159**, 151–168 (1985).